Spring 2024

Simulation of IC Circuits in Cylindrical Photoemission Driven Cavities using Coupled Monte Carlo and Particle-in-Cell Codes

Ravi Sanjay Shastri
Missouri University of Science and Technology

Department:

SIMULATION OF LC CIRCUITS IN CYLINDRICAL PHOTOEMISSION DRIVEN CAVITIES USING COUPLED MONTE CARLO AND PARTICLE-IN-CELL CODES

by

RAVI SANJAY SHASTRI

A THESIS

Presented to the Graduate Faculty of the

MISSOURI UNIVERSITY OF SCIENCE AND TECHNOLOGY

In Partial Fulfillment of the Requirements for the Degree

MASTER OF SCIENCE IN NUCLEAR ENGINEERING

2023

Approved by:

Ayodeji Alajo, Advisor
Syed Alam
Joseph Graham

ABSTRACT

This work presents a computational experiment simulating irradiation of gold in a cylindrical cavity. The full 3-D simulation with a B-Dot diagnostic is modeled, and a subset of the results are compared to modeling the system as a coupled anode/cathode (AK) gap and transmission line. The cavity is filled with N_2 and Ne gasses at pressures ranging from vacuum to 1000 mTorr. Space-charge limited emission physics, electric discharge physics, LC circuit physics, and Monte-Carlo methods are explored.

The computation process happens in two steps. First, the electron emission material is irradiated with an input x-ray photon spectrum to produce a photoelectron emission spectrum. This is accomplished using a Monte-Carlo photon-electron radiation transport code. The photoelectron spectrum, together with the x-ray time pulse and yield, is then used to characterize the electron emission into the gas filled cylindrical cavity that is modeled via an electromagnetic (EM) particle-in-cell (PIC) code. Each surface produces a different photoelectron emission spectrum and drives a current through the experiment that is measured in an output cavity. The effects of plasma dynamics, including plasma formation due to electron impact ionization within the cavity, are studied. Modeling the system as a coupled gas filled cavity and transmission line significantly reduces computational resources and provides accurate results. A transmission line was used to model the circuit of this geometry, and an axial configuration is shown to be a more viable method of modeling this geometry than a radial configuration. Finally, a comparison of different diagnostic geometries (a driven X-ray diode) is discussed.

ACKNOWLEDGMENTS

A special thank you to Peggy Christenson, Keith Cartwright, Adam Darr, and Scot Swan for helping me with the simulations and physics, and for being great mentors. I'd also like to thank Tim Flanagan for providing the time pulses, experimental data, x-ray yield data, and input photon spectrum and Sandia for providing the computational resources. A final thank you goes to my advisor, Dr. Ayodeji Alajo, and my committee members, Dr. Syed Alam, and Dr. Joseph Graham.

Sandia National Laboratories is a multi-mission laboratory managed and operated by National Technology & Engineering Solutions of Sandia, LLC, a wholly owned subsidiary of Honeywell International Inc., for the U.S. Department of Energy's National Nuclear Security Administration under contract DE-NA0003525.

This paper describes objective technical results and analysis. Any subjective views or opinions that might be expressed in the paper do not necessarily represent the views of the U.S. Department of Energy or the United States Government.

TABLE OF CONTENTS

Page

ABSTRACT iii

ACKNOWLEDGMENTS iv

LIST OF FIGURES vii

LIST OF TABLES xiii

NOMENCLATURE xiv

SECTION

1. INTRODUCTION 1

1.1. PULSED POWER EXPERIMENTS WITHIN AN AK GAP 1

1.2. B-DOT DIAGNOSTIC 2

1.3. PURPOSE OF THE EXPERIMENT 5

2. BACKGROUND INFORMATION 9

2.1. GEOMETRY OF THE CAVITY SIMULATION 9

2.2. PHOTOELECTRIC EFFECT 10

2.3. SPACE-CHARGE LIMITED CURRENT DERIVATION 12

2.4. CAVITY FILL GAS AND PRESSURES 15

2.5. LC CIRCUIT ANALYTICAL SOLUTION 17

2.6. MONTE CARLO METHODS 21

3. METHODS 23

3.1. EXPERIMENTAL SETUP 23

3.2. MONTE CARLO PHOTON/ELECTRON TRANSPORT CODE 28

3.3. EM PIC PLASMA PHYSICS CODE 33

3.4. EM PIC TRANSMISSION LINE MODELING 36

4. RESULTS 40
4.1. CONVERGENCE TESTING 40
4.2. BDL CURRENT OUTPUTS FOR FULL 3-D SIMULATION 42
4.3. SPACE-CHARGE LIMITED EMISSION 51
4.4. B-DOT OUTPUT FROM AXIAL TRANSMISSION LINE MODEL 54
4.5. TRANSMISSION LINE MODELING 59
4.6. EDL CURRENTS: VOLTAGE IN THE CAVITY 76
4.7. ELECTRIC DISCHARGE AND DOUBLE PEAKS 77
5. DISCUSSION 80
5.1. DRIVEN AK GAPS AND OTHER DIAGNOSTICS 80
5.2. COUPLING THE MC CODE TO THE EM PIC CODE 82
5.3. APPLICATIONS 83
6. CONCLUSION 84
APPENDIX 87
BIBLIOGRAPHY 91
VITA 93

LIST OF FIGURES

Page

Figure 1.1 B-Dot sensor circuit schematic. 2

Figure 1.2 Video of electron emission from the cavity geometry and current being sent through the B-Dot. 4

Figure 1.3 Comparison of current output for a transmission line simulation to experimental data. 5

Figure 2.1 15° wedge of the experimental setup with a B-Dot detector. 9

Figure 2.2 Electron count as a function of time in the cavity. 10

Figure 2.3 Photoelectric effect. 11

Figure 2.4 Different regions of current density emission behaviors. 15

Figure 2.5 Paschen curve for Ne. 16

Figure 2.6 Lumped element LC Circuit with capacitance C and inductance L. 17

Figure 2.7 Charge vs. time in the capacitor for an RLC damped circuit. 20

Figure. 2.8 Overdamped charge (line) and current (dashed line) as a function of time in the capacitor of an RLC circuit. 20

Figure 2.9 Gaussian distribution with different standard deviations and average values created by an MC method. 21

Figure 3.1 Flow chart of the experiment. 23

Figure 3.2 Photoelectron emission distribution due to stainless-steel photon radiation spectrum on the carbon coated aluminum foil. 24

Figure. 3.3 Photoelectron emission distribution due to stainless-steel photon radiation spectrum on unfiltered aluminum foil. 24

Figure 3.4 Visualization of a wedge of the cylindrical cavity at t = 11.4ns (N_2 fill gas, 100 mTorr, SCL on). 25

Figure 3.5 Sketch of the simplified 10 mm B-Dot photoemission cavity with dimensions. 26

Figure 3.6 3 ns FWHM x-ray pulse for stainless-steel wire array experimentally measured from the Z-Machine at Sandia. 27

Figure 3.7 1.5 ns FWHM x-ray pulse for silver spectrum experimentally measure from the Z-Machine at Sandia. 28

Figure. 3.8 Photoelectron output spectrum due to stainless-steel wire array x-ray irradiation in the stochastic photoelectron generator code in Au 29

Figure 3.9 Photoelectron output spectrum due to stainless-steel wire array x-ray irradiation in the stochastic photoelectron generator code in Ni 29

Figure 3.10 Heat map of photoelectron emission at different angles for Au (top) and Ni (bottom). 30

Figure 3.11 Photoelectron output spectrum due to x-ray irradiation from a silver source at NIF in the stochastic photoelectron generator code in Au. 31

Figure 3.12 Workflow of the EM PIC code. 34

Figure 3.13 Cavity with node sets highlighted in orange. 36

Figure 3.14 Simplified B-Dot geometry with finer meshes than the prebuilt geometry..... 37

Figure 3.15 Photoemission cavity with node sets highlighted in orange where the axial transmission line is modeled. 38

Figure 3.16 Photoemission cavity with node sets highlighted in orange where the axial transmission line is modeled. 38

Figure 3.17 Sketch of the simplified 1 mm B-Dot photoemission cavity with dimensions in mm. 39

Figure 4.1 Convergence testing data from the MC photon/electron code for surface 1. 40

Figure 4.2 Convergence testing data from ITS for surface 2. 41

Figure 4.3 Convergence testing data from the MC electron/photon code for surface 1 41

Figure 4.4 Convergence testing data from the MC electron/photon code for surface 2 42

Figure 4.5 Bdl Current vs time, Au B-Dot full simulation, vacuum. 43

Figure. 4.6 Bdl Current vs time for Ne between 200 and 500 mTorr for a 10 mm Au B-Dot system, with SCL emission toggled on/off. 43

Figure 4.7 Bdl Current vs time for Ne between vacuum and 200 mTorr for a 10 mm Au B-Dot system, with SCL emission toggled on/off. 43

Figure 4.8 Gas ionization cross-sections for N_2 and Ne gas [21]. 44

Figure 4.9 Bdl Current vs time for N_2 between 100 and 500 mTorr for a 10 mm Au B-Dot system, with SCL emission toggled on/off. 45

Figure 4.10 Bdl Current vs time for N_2 between vacuum and 200 mTorr for a 10 mm Au B-Dot system, with SCL emission toggled on/off.. 45

Figure 4.11 Direct comparison of Bdl Current vs time for Ne and N_2 fill gasses at low pressures. 46

Figure 4.12 Direct comparison of Bdl Current vs time for Ne and N_2 fill gasses at high pressures. 46

Figure 4.13 Direct comparison of Bdl Current vs time for Ne and N_2 fill gasses as a function of pressure. 47

Figure 4.14 Difference in current vs pressure for 100 mTorr pressure bins in Ne and N_2 with SCL off. 48

Figure 4.15 Difference in current vs pressure for 100 mTorr pressure bins in Ne and N_2 with SCL on. 49

Figure 4.16 Bdl Current vs time for Ne between 600 and 1000 mTorr for a 10 mm Au B-Dot system, with SCL emission toggled on/off. 49

Figure 4.17 Difference in current vs pressure for 100 mTorr pressure bins in Ne. 50

Figure 4.18 Bdl current vs time for Ne B-Dot simulations below 200 mTorr, SCL on/off, oscillatory. 52

Figure 4.19 Bdl current vs time for 10 mm Au B-Dot with N_2 fill gas with SCL toggled off. 52

Figure 4.20 Bdl current vs time for 10 mm Au B-Dot with Ne fill gas with SCL toggled off. 52

Figure 4.21 Bdl current vs time for 10 mm Au B-Dot with N_2 fill gas with SCL toggled on. 53

Figure 4.22 Bdl current vs time for 10 mm Au B-Dot with Ne fill gas with SCL toggled on. 53

Figure 4.23 Bdl current vs time for 10 mm Au B-Dot, Ne and N_2 gas comparison, SCL off. 53

Figure 4.24 Bdl current vs time for 10 mm Au B-Dot, Ne and N_2 gas comparison, SCL on. 54

Figure 4.25 First attempt at creating the cavity. The x-axis is oriented into the page, and the y-axis moves “left to right”. 56

Figure 4.26 Final geometry of the cavity. The x-axis moves “left to right”, and the y-axis is oriented into the page. 57

Figure 4.27 B-Dot transmission line segments, each section correlates with an LC value in Table 4.2. 58

Figure 4.28 Visualization of the diagnostics in the cavity. 59

Figure 4.29 Full geometry of 1 mm B-Dot. 59

Figure 4.30 Full geometry of 1 mm LB-Dot. 60

Figure 4.31 Bdl current vs time for a 1 mm B-Dot for pressures between 0 and 200 mTorr, full geometry, stainless-steel source. 61

Figure 4.32 Bdl current vs time for a 1 mm LB-Dot for pressures between 0 and 200 mTorr, full geometry, stainless-steel source. 61

Figure 4.33 1 mm B-Dot and LB-Dot photoemission cavity. 62

Figure 4.34 Bdl current vs time for a 1 mm vacuum B-Dot with the circuit modeled as an axial transmission line with different inductance values compared to the full simulation, silver source. 62

Figure 4.35 Bdl current vs time for a 1 mm vacuum LB-Dot with the circuit modeled as an axial transmission line compared to the full simulation, silver source. 63

Figure 4.36 Bdl current vs time comparing current outputs for normal and very reduced sensitivity. 64

Figure 4.37 Bdl current vs time for a 1 mm vacuum B-Dot with the circuit modeled as an axial transmission line with different inductance values compared to the full simulation, stainless-steel source. 65

Figure 4.38 Bdl current vs time for a 10 mm vacuum B-Dot with the circuit modeled as an axial transmission line with different inductance values compared to the full simulation, stainless-steel source. 65

Figure 4.39 Bdl current vs time for a 10 mm vacuum B-Dot with the circuit modeled as an axial transmission line with different inductance values compared to the full simulation, silver source. 66

Figure 4.40 Bdl current vs time for a 1 mm B-Dot with the circuit modeled as an axial transmission line at vacuum. 68

Figure 4.41 Bdl current vs time for a 10 mm B-Dot with the circuit modeled as an axial transmission line at vacuum. 69

Figure 4.42 Bdl current vs time for a 1 mm B-Dot with the circuit modeled as an axial transmission line with low-pressures of Ne fill gas.. 69

Figure 4.43 Bdl current vs time for a 1 mm B-Dot with the circuit modeled as an axial transmission line with low pressures of N_2 fill gas. 70

Figure 4.44 Bdl current vs time for a 1 mm B-Dot with the circuit modeled as an axial transmission line with high pressures of Ne fill gas..... 71

Figure 4.45 Bdl current vs time for a 1 mm B-Dot with the circuit modeled as an axial transmission line with high pressures of Ne fill gas..... 71

Figure 4.46 Bdl current vs time for a 1 mm B-Dot with the circuit modeled as an axial transmission line with low pressures of Ne fill gas. 72

Figure 4.47 Bdl current vs time for a 1 mm B-Dot with the circuit modeled as an axial transmission line with high pressures of Ne fill gas. 73

Figure 4.48 Bdl current vs time for a 1 mm B-Dot with the circuit modeled as an axial transmission line with high pressures of N_2 fill gas.. 74

Figure 4.49 Bdl current vs time for a 10 mm B-Dot with the circuit modeled as an axial transmission line with low pressures of Ne fill gas and a stainless-steel spectrum. 75

Figure 4.50 Bdl current vs time for a 10 mm B-Dot with the circuit modeled as an axial transmission line with low pressures of Ne fill gas and a silver spectrum. 75

Figure. 4.51 (left) Edl Current vs time for Ne between 200 and 500 mTorr for a 10 mm Au B-Dot system with SCL emission toggled on/off. 76

Figure 4.52 Edl Current vs time for Ne between 0 and 200 mTorr for a 1 mm Au LB-Dot (left) and B-Dot (right) system with SCL emission toggled on/off. 77

Figure 4.53 Bdl current vs time for N_2 and Ne B-Dot simulations between 0 and 200 mTorr with SCL on/off. 78

Figure 4.54 Bdl current vs. time for many materials (cathodes) with an N_2 fill gas, SCL on/off..... 79

Figure 5.1 DANTE II geometry..... 80

LIST OF TABLES

Page

Table 3.1 MC photon/electron code data showing uncertainty in each energy and theta bin 32

Table 4.1 Circuit model radial transmission line parameters 55

Table 4.2 L and C per unit length of each section of the transmission line circuit. G_l is conductivity, and the default is 0.0. 58

Table 4.3 L and C values for the axial transmission line..... 66

Table 4.4 L and C values for the axial transmission line..... 67

NOMENCLATURE

Symbol	Description
SNL	Sandia National Laboratories
AK	Anode / Cathode
SCL	Space-Charge Limited
EM PIC	electromagnetic particle-in-cell
MC	Monte-Carlo
NIF	National Ignition Facility
mTorr	millitorr
PDFs	Probability Density Functions
CDFs	Cumulative Density Functions
Ne	Neon Gas
N_2	Nitrogen Gas
Au	Gold Foil
Ag	Silver
Al	Aluminum Foil
Ni	Nickle
$\dot{\vec{B}}$	Changing Magnetic Field
C	Capacitance
L	Inductance
$\bar{\mu}$	Electron Mobility
ω	Resonant Frequency

β	Oscillation Parameter
RLC	Resistor, Inductor, Capacitor
LC	Inductor, Capacitor
SS	Stainless Steel
mm	millimeter
am	micrometer
nm	nanometer
keV	Kilo-electron volts
MeV	Mega-electron volts
v	Velocity
q	Charge
J	Current Density
I	Current
V	Voltage
h	Planck's Constant
ν	Frequency
m	Mass of an electron
d	Gap size
p	Pressure
γ_{se}	Secondary Electron Emission Coefficient
A	Electron emission surface area
ε_0	Permittivity of free space
μ_0	Permeability of free space

ε_r	Relative Permittivity
μ_r	Relative Permeability
ρ	Charge Density
c	Speed of Light
TL	Transmission Line
nH	Nano-Henry
nF	Nano-Farad
XRD	X-ray Diode

1. INTRODUCTION

1.1. PULSED POWER EXPERIMENTS WITHIN AN AK GAP

Pulsed power experiments performed on the Z Machine at Sandia National Laboratories (Sandia or SNL) are essential to understanding radiation effects on electrical equipment. The Radiation Effects Sciences team researches these effects experimentally and computationally. The physics effects of pulsed photon irradiation of materials from pulsed power experiments can be calculated computationally using many in-house Monte Carlo (MC) and particle-in-cell (PIC) codes.

This computational experiment involves the irradiation of a material in an anode/cathode (AK) gap by an x-ray pulse and studies the effects of the incident radiation. First, the electron emission material is irradiated with an input x-ray photon spectrum to produce a photoelectron emission spectrum. This is accomplished using a stochastic radiation transport code. The photoelectron spectrum, together with the x-ray time pulse and yield, is then used to characterize the electron emission into the gas filled cylindrical cavity that is modeled via an electromagnetic (EM) PIC code. The EM PIC code solves Maxwell's equations in the presence of charged particles to self-consistently model the electromagnetic plasma dynamic evolution within the AK gap.

The motivation behind this thesis is understanding harsh radiation environments effects on electrical equipment. Simulating these environments is of great importance to national security, as it ensures valuable assets will function properly in harsh radiation environments. Sandia is home to the Z Machine, the world's most powerful pulsed power accelerator, as well as HERMES, SPHINX, and SATURN, which can all create these

harsh environments on nanosecond timescales. Having this data available is instrumental for model verification, as we can compare our simulations to experiments. Simulations provide good estimates of the behavior of the system, and models are continuously being updated with data from pulsed power shots.

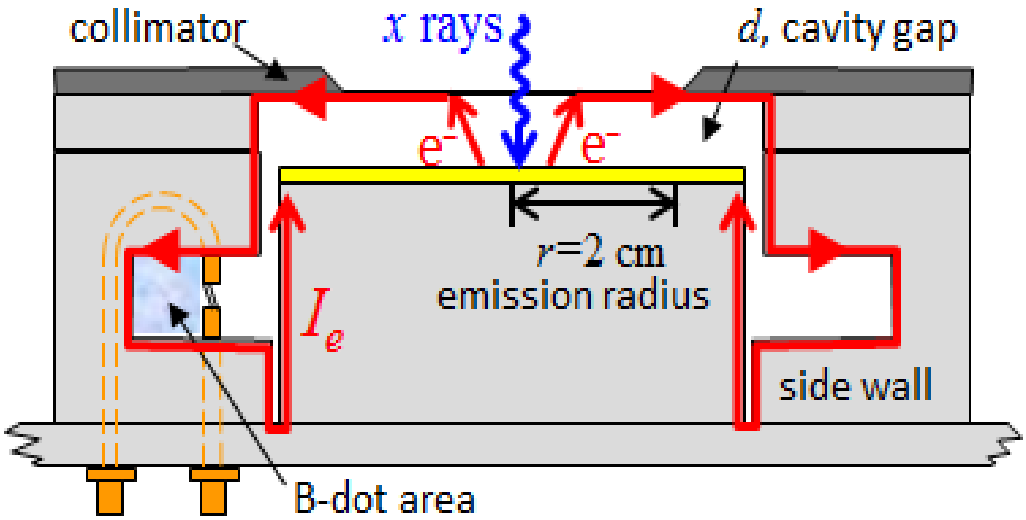

Figure 1.1 B-Dot sensor circuit schematic. The pulse creates a current, which induces a magnetic field in the sensor circuit, producing a voltage in the sensor circuit [3].

1.2. B-DOT DIAGNOSTIC

In harsh radiation environments, it is essential to know how much current flows through an AK gap so as not to destroy the electrical equipment. The objective of this work is to calculate the amount of current through a circuit as a function of time after photo-irradiation. The source of these photons can be a monoenergetic beam or a spectrum of photons from experiment. The current measurement diagnostic used in our cylindrical end; irradiated cavity experiment is called a B-Dot [2]. The name B-Dot comes from the physics expression $\dot{B}$, the time-varying magnetic field (B) induced in the

circuit, more commonly written as dB/dt [3]. Simulation of B-Dot output from x-ray irradiation of the experimental cavity has many practical applications in science, engineering, and nuclear deterrence. A visualization of the cavity experiment is shown in Figure 1.1.

There are two surfaces that emit photoelectrons in this cavity: the top surface and the bottom surface. The anode is the top surface (where x-rays enter the system in Figure 1.1), and it is composed of aluminum with a 5μm carbon coating. The carbon coating suppresses current emission. Other filters, such as lithium and Kapton could be added, but the carbon filter is sufficient for this simulation. This is surface 1 in our system, or the top of the cavity in Figure 1.1. Surface 2 is the bottom surface (the yellow line in Figure 1.1 that emits electrons). This is the cathode, and it has a higher photoelectric emission intensity than the anode. In this experiment, our cathode is gold, but other popular cathodes include silver, molybdenum, and yttrium. The cathode has at least an order of magnitude higher emission intensity than the anode, so we can ignore the photoelectric contribution from the anode with only a small loss in resolution. This would not be viable without filters suppressing photoelectric emission. After irradiation, current flows along the red lines in Figure 1.1 and induces a current in the B-Dot. The B-Dot outputs a time-varying voltage that we can easily convert to current. Understanding Figure 1.1 is essential to understanding the physics of this simulation, and we will refer to it many times throughout the paper.

The experiment explored in this work is a computational simulation of a B-Dot output where only the B-Dot geometry is modeled. Current through the B-Dot for different fill gasses and pressures is calculated and plotted, and important comparisons of

fill gasses and pressures are made. The second part of this experiment models the geometry in two parts: the cavity, where plasma physics drive the current, and a transmission line. The transmission line is a substitute for modeling each individual component of the B-Dot, the goal is to reproduce the current output in the B-Dot with a transmission line model. The physics of the geometry is still modeled, but there can be a simplification by modeling the B-Dot as a transmission line. The simulated current can be compared to the processed experimental B-Dot measurements. The most important physics of this experiment are currents in the B-Dot ($\mu_0 I = \int \vec{B} \cdot d\vec{l}$ or "Bdl" current from Ampere's law, integrated over the B-Dot cavity walls) and space-charge limits on currents. Additionally, the fill gas type and pressure, irradiation material, anode filter stack, and distance from the detector can be varied, but that is beyond the scope of this project.

A video showing the electron emission as it traverses the gap and goes through the B-Dot is shown below. After the photon irradiation of the A/K gap, the blue particles represent electron emission from the cathode. The electrons then are transported though the circuit, and Bdl current is read in the B-Dot.

Sandia_CollimatorParticles_20200603.mp4

Figure 1.2 Video of electron emission from the cavity geometry and current being sent through the B-Dot. Double-click to play the video.

1.3. PURPOSE OF THE EXPERIMENT

During October of 2022, a series of shots were taken on the Z machine at Sandia. Some of these shots involved measuring the photoelectric current caused by the warm x-ray irradiation of a material (Au and Ni) in a cylindrical end cavity with an AK gap. The goal of that work was to predict the magnitude of the current in the B-Dot detector using the EM PIC code and compare the results to the shots. To do that, we needed to couple the EM PIC code with a Monte Carlo (MC) photon-electron code to generate the photoelectron emission spectrum from the irradiated material.

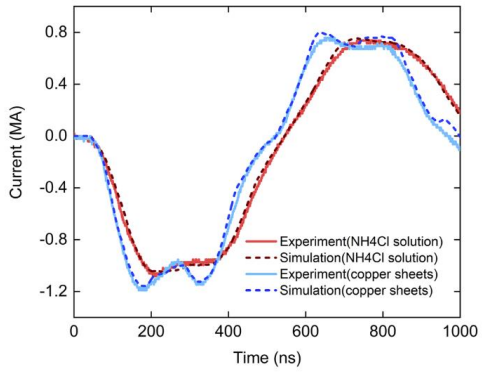

Figure 1.3 Comparison of current output for a transmission line simulation to experimental data. Inductance of the transmission line was matched to the inductance of the original solution and volume [5].

Using the EM PIC code to model the entire geometry simultaneously is a valid approach. However, by choosing to model the system as two parts – the cavity and the stem – computational resources can be greatly reduced without sacrificing accuracy and physics. The assumption is that the stem and the B-Dot is just and electromagnetic

circuit. If this is true, coupling the AK gap, and its relevant plasma physics, to the transmission line should allow for finer meshes and fewer computer hours. It has been shown that modeling this geometry as an RLC (resistor, inductor, and capacitor) circuit or an LC circuit is possible, producing similar results [4]. Another study directly compared experimental results to a simulated transmission line brought in radially, as further proof of this concept [5].

The experiment, performed by Tim Flanagan [4], was for irradiated gold, with a gap size of 1 mm and no fill gas (vacuum). Different values for inductance and capacitance were explored by varying the geometry. Without a fill gas, the vacuum system was able to be modeled as an RLC circuit. More information on underdamped oscillators can be found in reference [6]. However, as well as a 1 mm photoemission driven cavity, the system of interest in this thesis is a 10 mm photoemission driven cavity, still with gold as the irradiated material, but with pressures between vacuum and 1 Torr (Ne and N_2 fill gasses respectively). Because the incident photon spectrum (the blue x-ray input in Figure 1.1) is of sufficient energy, the fill gasses become ionized, resulting in plasma formation within the cavity. The plasma means we cannot model gas-filled AK gaps as an RLC circuit but must instead use the EM PIC code. Modeling the entire system is computationally expensive. It can take many hours and many nodes (computational resources) to model the physics of the photoemission-driven cavity alone. Fortunately, we may break up our geometry into two parts and build a separate model for each. The plasma-containing gap is modeled with the EM PIC code, while the stem is modeled much more cheaply (more quickly, using only one node in vacuum cases) as an RLC or LC circuit (as mentioned above, the gap and the stem).

As an input, we use both a stainless-steel x-ray spectrum through a carbon filter from the Z-Machine or a silver x-ray spectrum from the National Ignition Facility (NIF). Both spectra come from experimental data and is of paramount importance in generating an accurate photoelectron output spectrum from the MC photon/electron code. They are incident upon a gold foil in the cavity. When the entire cavity is modeled, we will focus on the stainless-steel input spectrum because it is less oscillatory after the initial pulse. Modeling the transmission line is much easier for a silver spectrum because we see oscillations after the initial time pulse, which allows us to find LC much easier. This will be explored in more detail in the Results section. The AK gap is 10 mm and is filled with Ne or N_2. The pressure is varied between 0 and 1000 mTorr in 100 mTorr increments, and Bdl current is measured. These simulations allow us to see the difference in modeling space-charge limiting current effects versus neglecting them, and determine the peak current induced in the B-Dot. The comparison of N_2 and Ne fill gasses in the cavity will show the differences in the gasses ability to withstand electric discharge at different pressures. At pressures close to the point of maximum electric discharge we can see double peaks. The differences in the minima of the Paschen curves (breakdown voltage vs. pressure * gap distance) for each gas will be relevant, and we can make this comparison for many materials (Au, Ag, Ni, It, Mo, Y, etc.) However, this work will focus on the gold cathode due to its high photoelectric emission.

In this work, we will explore the physics of a B-Dot diagnostic, space-charge limited emission (SCL) currents, the minimum ionization voltage for Ne and N_2, the analytical solution to lumped element LC circuits, and basic MC methods. We will also explore computational techniques used at Sandia National Laboratories. We will use

coupled MC and PIC codes to generate photoelectric spectra, perform convergence testing of the MC photon/electron code. Finally, using visualization tools such as CUBIT, ParaView, and gnuplot, we will visualize geometry dimensions and meshing and Bdl current outputs. Finally, the results from previous AK gap simulations with NE and N_2 fill gasses respectively will be compared to simulations where a transmission line takes the place of a B-Dot. The differences between bringing in the transmission line radially (equidistant from the center) and axially (same $\hat{z}$ coordinate) will be discussed. Different parameters for L and C of the transmission line will be modeled, and eventually, the oscillation frequency of the tail of the pulse can be used to analytically fit LC values to the transmission line per unit length. Discussing the viability for different diagnostics will also be discussed.

Another benefit of modeling a transmission line in place of a B-Dot diagnostic comes from its interchangeability. In other diagnostics, ones where the return circuit is more complex than a B-Dot, it can be cumbersome to model the full circuit path. Modeling a transmission line in place of the return circuit can reduce complexities associated with modeling the full geometry, while producing similar output physics. This method will also reduce the computational resources required to transport particles through the diagnostic.

2. BACKGROUND INFORMATION

2.1. GEOMETRY OF THE CAVITY SIMULATION

Building the geometry of the cavity in the simulations is critical to getting accurate predictions about current outputs. However, modeling every aspect of the cavity is overly complex, possibly leading to unnecessary computational expense; we can simplify the model and obtain similarly accurate results. The cavity used for this simulation is a cylindrical, end irradiated current driven cavity with currents driven by photoelectron emission. A fifteen-degree wedge of the cavity, stem, and detector is modeled in CUBIT and meshed. Its mesh and geometry are and imported into the EM PIC code, and azimuthal symmetry can be assumed.

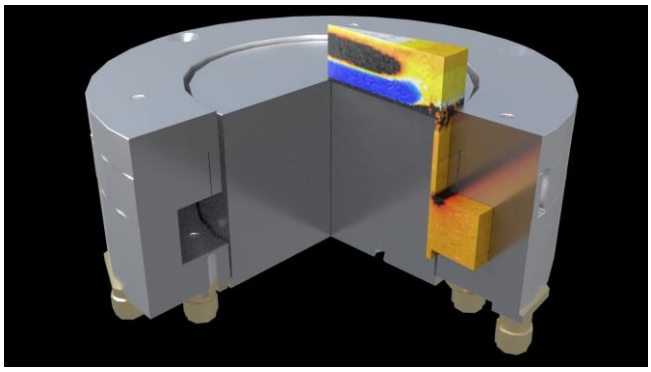

Figure 2.1 15° wedge of the experimental setup with a B-Dot detector.

Finally, the sensor cavity radius is sorted into three categories: N type, R type, and V type (normal, reduced, and very reduced respectively). N type geometries have a sensor radius of 35mm, R type geometries have a sensor radius of 32.5mm, and V type

geometries have a sensor radius of 30.5mm. We should see a slight change in Bdl current output because of this small change in radius. We will focus on Au N type geometries for the full simulation, and V type geometries for the transmission line solutions, because they peak slightly earlier, and have slightly higher current outputs. However, the difference between these Bdl current outputs is small.

A video of the electric field in the cavity and the B-Dot is shown below. The geometry is a wedge of Figure 2.1 with electric field shown as a color gradient. After the photon irradiation, there is a large amount of electron emission from the cathode. There are many of electrons in the B-Dot post irradiation, as shown in the video. Electron emission in the cavity is highly space-charge limited, until the plasma drives more current through the B-Dot, as seen by a visible blue region for a long time before the plasma causes that SCL region to disparate. This is known as the Schottky effect [7].

bdot_electon_final.mp4

Figure 2.2 Electron count as a function of time in the cavity. Double click to play the video.

2.2. PHOTOELECTRIC EFFECT

Albert Einstein's contributions to physics go much deeper than just relativity. He contributed to atomic physics by studying laser physics before a laser was even invented, he studied statistical mechanics, but most importantly for this work, he discovered the photoelectric effect. Einstein concluded that light was composed of quanta (photons), and quantum mechanics was born [8].

The photoelectric effect occurs when a photon of a specific frequency hits a metal surface, subsequently causing an electron to be released. Figure 3 is an illustration of this phenomenon.

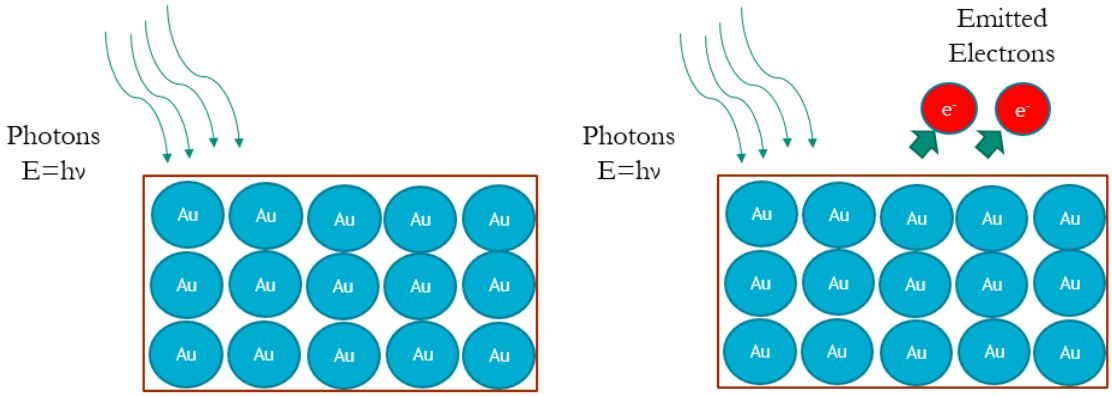

Figure 2.3 Photoelectric effect. Photons at a given energy are incident upon a metal, which causes and excitation and the subsequent the release of electrons, called photoelectrons. Not drawn to scale.

In the illustration, the photons have energy E = hν, where h is Planck's constant and ν is the frequency of the photons. Every material has "resonances" where photons of specific energies cause most of the photoemission. Thus, the specifics of a photon spectrum and the specifics of an irradiated material combine to determine overall emission characteristics. This will be explored in further depth in the methods section. The photons in our experiment from the stainless-steel spectrum are warm x-rays that range from 1 keV (1.2398 nm wavelength) to 20 keV (0.0620 nm wavelength). The photons from the silver spectrum range from 1 keV to 32.2keV (0.0385 nm wavelength). Photoelectric emission intensities are divided into energy bins, and the emission strength

is tallied in the MC electron/photon code. This shows us at what energies dominate photoelectric emission for each material, and the strength of that emission.

2.3. SPACE-CHARGE LIMITED CURRENT DERIVATION

It is important to understand the physics of space-charge limiting (SCL) currents before analyzing the simulations. Although the EM PIC solves the three-dimensional, non-linearly coupled charged particle dynamic equations to Maxwell's equations numerically, we may turn to theory for a general idea of SCL effects. We will start by picturing a parallel plate capacitor that has variation only in $\hat{z}$ and has charge $\pm$Q (positive charge on the upper plate, negative charge on the lower plate) [9].

For a parallel plate capacitor, $Q = AV\varepsilon_o/d$, where A is area of each plate, ε_o is the permittivity of free space, V is voltage, and d is the distance between the plates.

The average velocity of the electrons as they cross the gap must be somewhere between 0 and v_{max}, the maximum electron velocity. For simplicity, we will assume that the average velocity $\bar{v}$ is half of the maximum velocity [9], such that

$$\bar{v} = \frac{v_{max}}{2}. \tag{1}$$

From conservation of energy, we know that $v_{max} = \sqrt{2eV/m}$, where m is the mass of an electron. The current traversing the gap can be expressed as $I = Q\bar{v}/d$, so the current and current density are given by

$$I = \frac{\epsilon_0 AV}{2d^2}\sqrt{\frac{2eV}{m}}; \quad J = \frac{\epsilon_0}{2d^2}\sqrt{\frac{2e}{m}}V^{3/2}. \tag{2}$$

When comparing our derivation to the Child-Langmuir law

$$J_{SCL} = \frac{4\varepsilon_0}{9d^2}\sqrt{\frac{2e}{m}}V^{3/2}, \tag{3}$$

we realize that the coefficient changes from 1/2 to 4/9 [10]. Thus, our simple derivation gives a good sense of SCL physics. Current scales as voltage to the three-halves power, and inversely with gap distance squared.

From the Child-Langmuir equation (3), we can find the relationship between distance between the electrodes in the B-Dot cavity and voltage across the cavity. Physically, the SCL current represents the maximum current that can be transmitted across an anode cathode gap. It corresponds to a surface electric field of zero when electrons have zero initial velocity, where any additional emission would be rejected back into the cathode due to the "shielding" effect of the electron charge density in the gap.

The Child-Langmuir equation is for a parallel plate gap. This is not quite the geometry in our simulation: we are looking at a cylindrical end-irradiated photoemission driven cavity with a fill gas. The cavity gap geometry resembles a parallel plate capacitor; however, there are non-insignificant edge effects from the entrance to the stem of the geometry. The fill gas will reduce the velocity of the electrons traversing the gap, even when compared to the actual average velocity from the full Child-Langmuir derivation. Since the electrons will thus spend more time in the gap, Child-Langmuir equation (3) will overpredict the current in the B-Dot for these conditions. However, plasma formation reduces the electric field, which could mean Child-Langmuir underpredicts instead.

Let's consider the one-dimensional cylindrical end irradiated cavity (no edge effects) under irradiation of a cold (monoenergetic) beam of electrons of energy 5 keV.

The average energy of the stainless-steel wire array is around 5 keV, so solving for current will give us a ballpark estimate of what our current output should be. We know that J is the current density, and JA = I, where A is the area of the emission surface. Using the Child-Langmuir law, we can expect the space-charge limited current to be around 1000 amps in a 1 mm cavity, and 10 amps in a 10 mm cavity. However, our simulation is much more complex. We will be using a spectrum of photons, our anode also emits some electrons, our cavity is not a one-dimensional system, and we see significant edge effects.

When a fill gas is added, we expect to see ionizing collisions that create a plasma in the gap. However, not all collisions will be ionizing; there will be some collisions that are non-ionizing, and those can prevent the emitted electrons from traversing the gap and contributing to the current output. At higher pressures, the current density is not limited by only SCL emission, but also Mott-Gurney limited current, which scales $J \propto \frac{V^2}{D^3}$. The non-ionizing collisional electrons move at the electron drift velocity and contributes to a lower current density at higher pressures, or the change in peak current per pressure decreases as pressure increases. The Figure below shows where the Mott-Gurney and SCL emission regions are, plotted as voltage as a function of electron mobility [11]. Voltage is plotted as a function of electron mobility, $\bar{\mu}$. As shown in the Figure, the low electron mobility and low voltage region is governed by Mott-Gurney current density, the high mobility and low voltage region is governed by Fowler-Nordheim current density, and the high voltage region is governed by the Child-Langmuir law, with some regions in between for transition regions [7]. For more information about ionizing and non-ionizing collisions, see references [7] and [11].

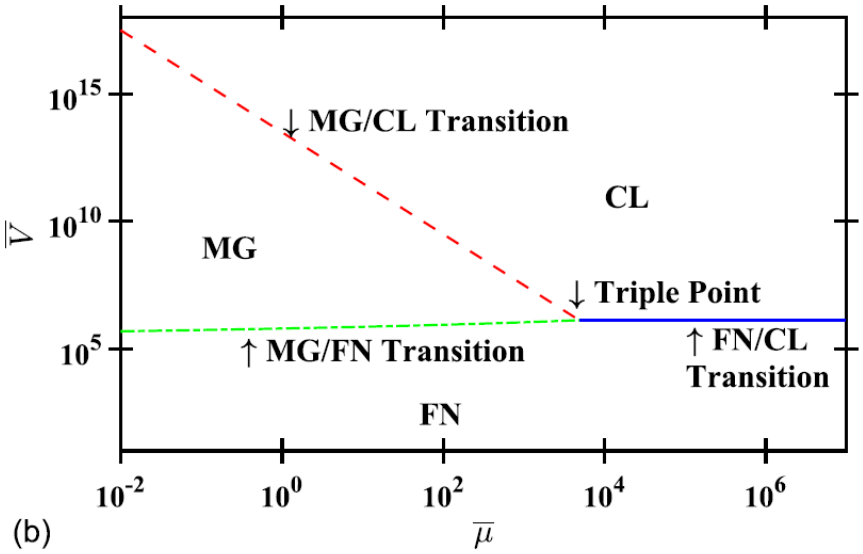

Figure 2.4 Different regions of current density emission behaviors [11].

2.4. CAVITY FILL GAS AND PRESSURES

As the pressure increases in the cavity, we expect that the Bdl current will increase when significant plasma is present, but possibly decrease if the plasma is suppressed and only non-ionizing electron-gas collisions take place. For some gasses, we see pressure Bdl current decrease as a function of pressure after surpassing a given pressure. This phenomenon can be explained by the pressure in the cavity being too high to generate as much plasma as in lower pressure cases for some gasses, especially N_2. Figure 2.2 shows the Paschen curve, which shows the voltage necessary for electric discharge in a gas. Equation 4 shows the voltage as a function of pressure, where V_d is voltage, p is pressure, d is gap size, γ_{se} is the secondary electron emission coefficient, A is the saturation ionization coefficient, and B is the coefficient related to the ionization energy of each gas [12].

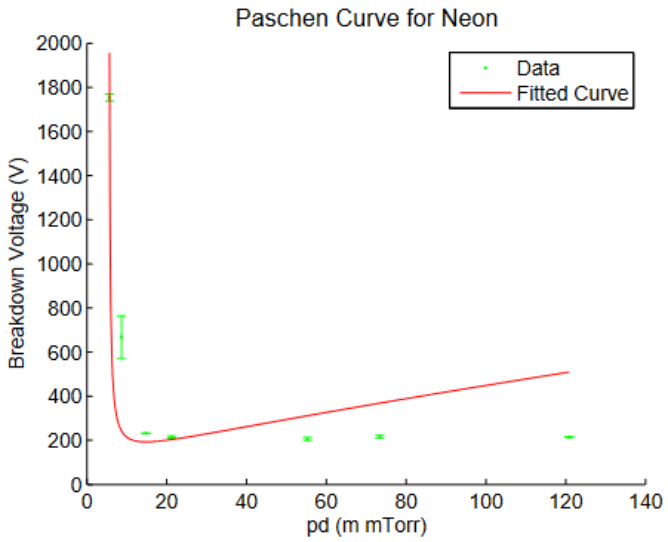

Figure 2.5 Paschen curve for Ne. This shows the voltage required for electric discharge as a function of pressure. N_2 and Ne are explored in this paper [13].

$$V_B = \frac{Bp\,d}{ln(Apd) - ln\left[ln\left(1 + \frac{1}{\gamma_{se}}\right)\right]} \tag{4}$$

As the pressure changes, the amount of energy available for ionization changes as collisions become more frequent and electrons gain less energy between collisions. There is a clear minimum at lower pressures. After the minimum, pressure increases correlate to more voltage required for ionization of the gas. We will see that in a current vs. pd curve, the current increases to a maximum and then decreases as a function of pressure (at constant gap distance). We will see these results when comparing Ne and N_2 fill gasses. Regardless of the fill gas, turning on SCL effects will drive a current through the cavity long after the initial x-ray pulse.

2.5. LC CIRCUIT ANALYTICAL SOLUTION

Let's consider a single loop circuit that follows Kirchhoff's voltage law. The circuit is not driven ($V_0 = 0$), the capacitance and inductance are L and C respectively, and the capacitor has an initial charge q_o. Although there could be many capacitors, since we are working in series, we lump these capacitances together into one equivalent capacitance. Figure 2.3 shows the circuit model [14].

$$\sum V = \oint_C \vec{E}\, d\vec{l} = 0 \tag{5}$$

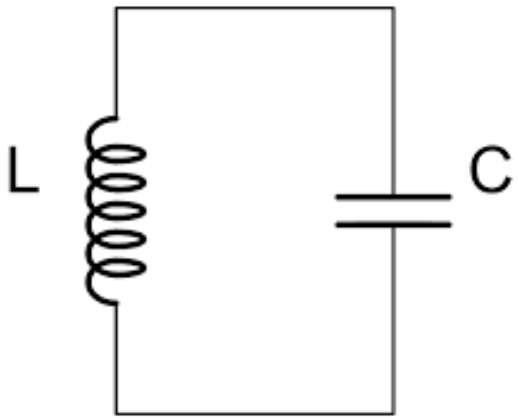

Figure 2.6 Lumped element LC circuit with capacitance C and inductance L [15].

where *V* is the voltage across each element. We know from Kirchhoff's voltage law that the total voltage in a closed loop is zero. We also know that $V_0 = \varepsilon$, $V = qC$, and $V_L = L dI/dt$, where q is charge, and I is current. The voltage for each term is

$$V_0 - V_c - V_L = 0, \text{ or } V_0 = V_c + V_L, \text{ and } \varepsilon = qC + L\frac{dI}{dt}. \tag{6}$$

Since the circuit is not driven, $\varepsilon = 0$, the current as a function of time is just the rate of change of the charge within the circuit: $I(t) = \frac{dq(t)}{dt}$. Combining these equations yield the simple 2nd order differential equation for a harmonic oscillator,

$$\left(\frac{d^2}{dt^2} + \frac{1}{LC}\right) q = 0 \tag{7}$$

with resonant frequency

$$\frac{1}{LC} = \omega^2. \tag{8}$$

Solving equation 7, and taking its derivative to find I(t), we have

$$q(t) = A\cos(\omega t) + B\sin(\omega t) \tag{9}$$

and

$$I(t) = -A\,\omega\sin(\omega t) + B\,\omega\cos(\omega t). \tag{10}$$

The initial conditions are $q(t=0) = q_0$, and $I(t=0) = 0$. Therefore,

$$q(t) = A = q_0 \tag{11}$$

and

$$I(t) = B\omega = 0; \omega \neq 0, \text{ therefore } B = 0. \tag{12}$$

Plugging in A and ω, we have our final solution for q(t) and I(t)

$$q(t) = q_0 \cos\frac{t}{\sqrt{LC}} \tag{13}$$

and

$$I(t) = \frac{-q_0}{\sqrt{LC}}\sin\left(\frac{t}{\sqrt{LC}}\right). \tag{14}$$

The solution to this circuit is a simple sinusoidal function.

A more interesting problem is where the LC circuit is driven ($V(t=0) = V_0$), and $q_0 = 0$. There, the particular solution is given by $q_p = CV_o$ [16], and the circuit equations are

$$q(t) = -CV_0 \cos\frac{t}{\sqrt{LC}} + CV_0 \tag{15}$$

and

$$I(t) = CV_0 \sin\frac{t}{\sqrt{LC}}. \tag{16}$$

This derivation is beyond the scope of this thesis, but one can perform this derivation starting with equation (6) and setting $\varepsilon = V_0$.

Finally, the resistor is a first order dampening term. From Kirchhoff's law, we can write

$$\varepsilon = qC + \mathrm{IR} + L\frac{\mathrm{d}I}{\mathrm{d}t}, \tag{17}$$

where $V_{resistor} = IR$ (Ohms law). This derivation is performed in chapter 13.3 of Reference [16], and has the following behavior.

The dampening of a circuit depends on β, the dampening coefficient of the circuit. If $\beta < i\omega$, the circuit is underdamped., and we see some oscillations before the charge in the capacitor dissipates. If $\beta < i\omega$, the circuit is critically dampened, and we will see no oscillations in the I(t) or q(t) graphs in the capacitor. The dampening comes from energy loss through heat in the resistor. Below are examples of underdamped and critically damped cases [16].

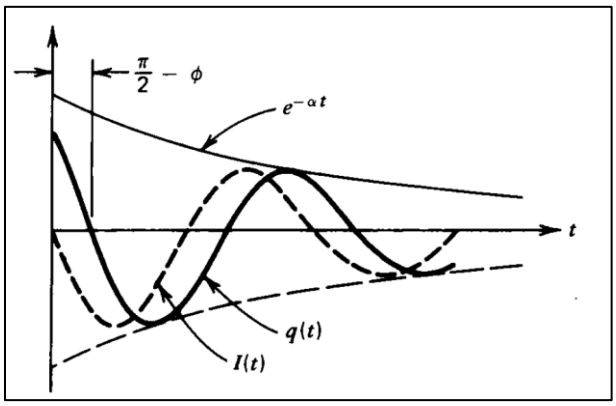

Figure 2.7 Charge vs. time in the capacitor for an RLC damped circuit [16].

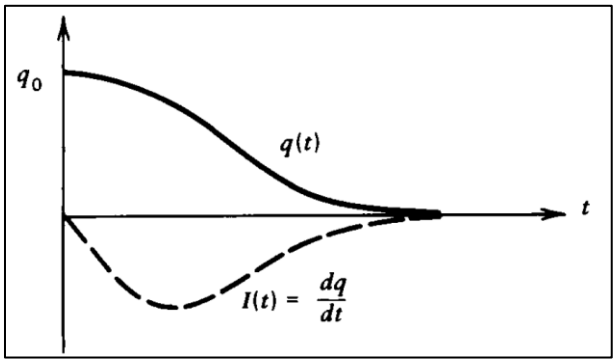

Figure. 2.8 Overdamped charge (line) and current (dashed line) as a function of time in the capacitor of an RLC circuit [16].

The dampening comes from the resistor. In our photoemission driven cavity, we have the option to model or ignore SCL emission. When we do model SCL emission, we notice a smooth tail after the pulse, as opposed to an oscillatory tail from the SCL off case. This is because the plasma in the cavity overdamps the circuit, and the oscillations are non-existent as the current decays.

2.6. MONTE CARLO METHODS

An MC simulation uses random sampling to estimate mathematical functions and mimic the operations of complex systems; in our case, photoelectric radiation transport [17]. A general pattern for MC simulations is to model a system as a series of probability density functions (PDFs), sample from the PDF many times, and tally the results [17]. The code generates a random number that corresponds to the probability of an event occurring. Although true randomness is impossible to create computationally, many algorithms generate numbers that are close enough to being random for most MC purposes. The process repeats many times for each particle until it leaves the system or "dies", the result is tallied, and the process repeats many times.

The integral of the PDF is the cumulative distribution function (CDF), which gives the probability that a randomly sampled number from the PDF will be less than or equal to the given value, x [17]. These CDF's can follow many distributions, including Poisson and Gaussian distributions. Below is a Gaussian with different standard deviations generated using an MC simulation.

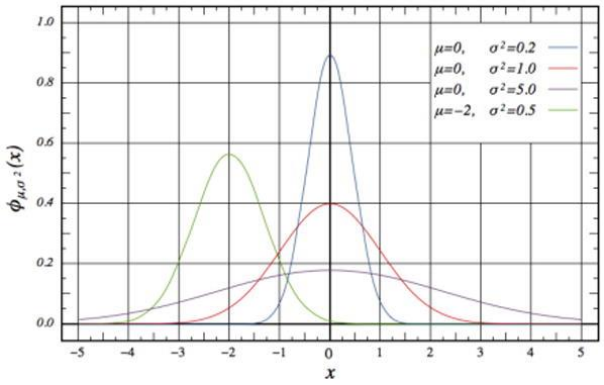

Figure 2.9 Gaussian distribution with different standard deviations and average values created by an MC method [17].

The simulations below use over 10^9 particles. MC methods, although time consuming, should provide similar results to experiment (assuming accurate models), and allows us to solve problems that would be difficult to solve analytically. Another sampling method is the method of characteristics, which creates tracks that particles follow to find the behavior of a system. This method is generally quicker but can lack accuracy.

3. METHODS

3.1. EXPERIMENTAL SETUP

There are two major steps to the simulation: the electron/photon MC transport code that is used as a stochastic photoelectron spectrum generator, and the EM kinetic plasma PIC code. Figure 3.1 is the workflow of the simulation.

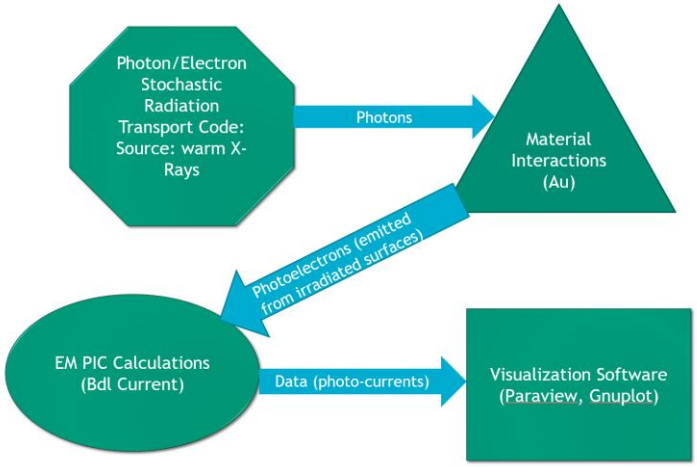

Figure 3.1 Flow chart of the experiment. Coupled simulation between two codes.

The input photon spectra used in these experiments are from a stainless-steel Z-pinch wire array, or a silver source from NIF. A stack of filtering materials is added to filter out low energy photons and keep only the higher energy x-rays. The x-rays are computationally transported through an aluminum foil that seals the gap allowing the pressure to be held at vacuum or at a low gas pressure. The foil is coated on the AK gap-facing side (top surface in Figure 1.1) with a thin layer of carbon (.005mm) to suppress

photoelectron emission from the foil into the gap. The output of the MC code is a normalized photoelectric emission spectrum. The x-axis in Figure 3.2 is energy in MeV, and the y-axis is photoelectron emission intensity as a function of energy.

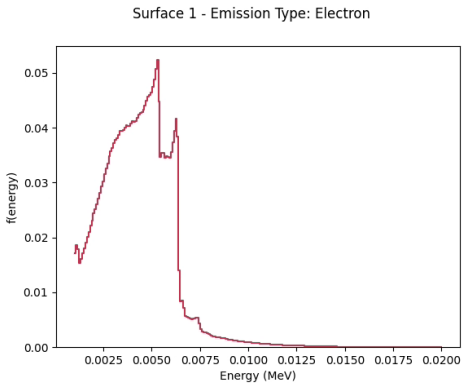

Figure 3.2 Photoelectron emission distribution due to stainless-steel photon radiation spectrum on the carbon coated aluminum foil.

Without the carbon filter, the emission spectrum is very different. The emission is much higher from the anode, and we cannot treat the system as a single surface emitter.

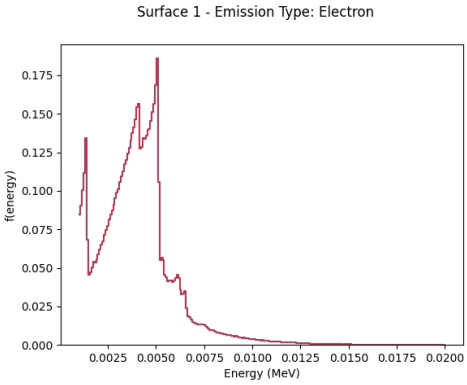

Figure. 3.3 Photoelectron emission distribution due to stainless-steel photon radiation spectrum on unfiltered aluminum foil.

The geometry of the cavity is produced such that the gap size is set to one or ten millimeters. The spectra are used to simulate a current, measured in the simulation with the integral of Bdl with the path in the theta direction, which can be compared to an experimentally measured B-Dot. The stainless-steel wire array spectrum has data for photons between 1 keV and 20 keV, and the silver spectrum has data between 1 keV and 32 keV. The MC photon/electron code struggles to model photons below 1 keV, so starting at 1 keV makes sense for this simulation.

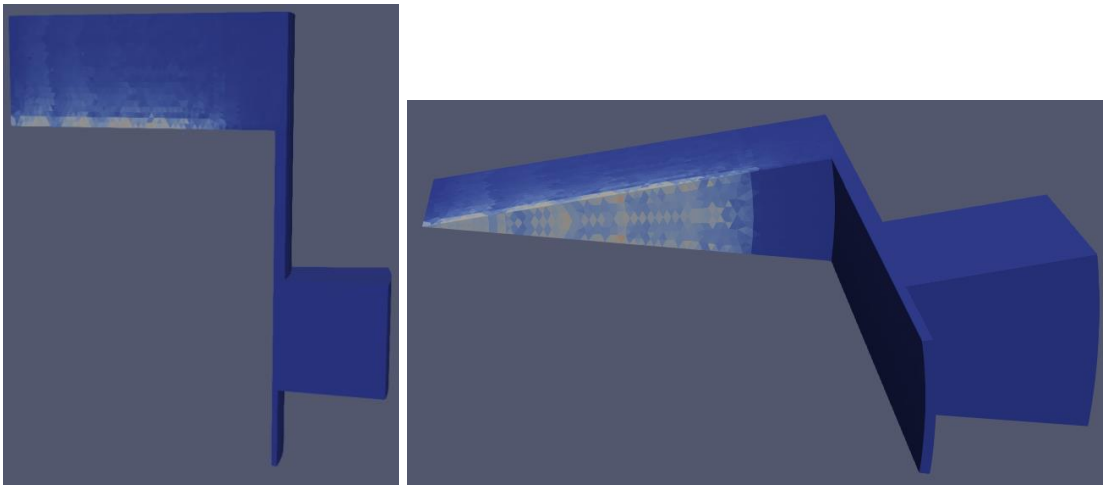

Figure 3.4 Visualization of a wedge of the cylindrical cavity at t = 11.4ns (N_2 fill gas, 100 mTorr, SCL on). On the right, we have a profile view of the system. The top and bottom surface of the cavity are colored white because that is where photoelectron emission is. The blue block on the right is the B-Dot diagnostic. On the left, we have a clearer view of the electron emission at the cathode.

Simulating the system as an AK gap with a coupled transmission line allows us to simplify the geometry very easily. In some situations, it is unnecessary to model the entire return circuit of the diagnostic when it can be simplified as a transmission line. This work will explore this simplification and see if the outputs of the full simulation can

be replicated in the transmission line simulation and see if the computational resources savings are worth the sacrificed physics. The photoemission cavity can be modeled as is, but we can get rid of the stem and the B-Dot sensor cavity. Below is a sketch of the simplified system where the transmission line was brought in axially.

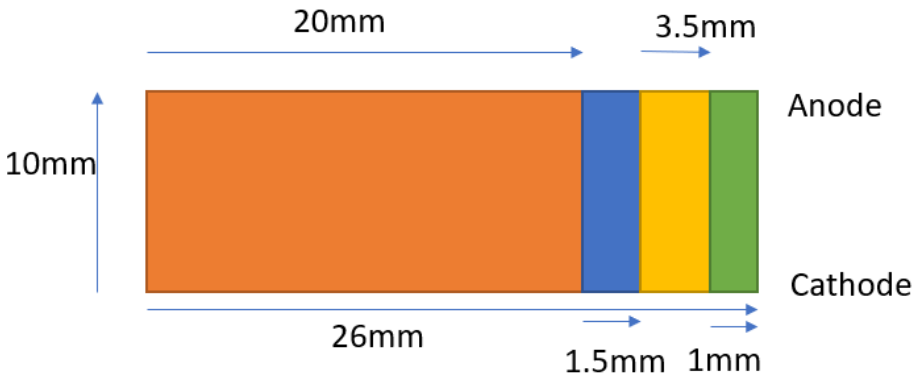

Figure 3.5 Sketch of the simplified 10 mm B-Dot photoemission cavity with dimensions. The orange region is the photoemission region, with the top and bottom surfaces being the AK gap. All the distances are radii, and they are reflected about the far left of the sketch (like Figure 1.1). Photons come in from the top.

The Al and Au foils (surfaces 1 and 2 respectively) extend 25mm, or across the entire photoemission cavity, and they even wrap around the edges a little bit. However, we do not expect photoemission in the yellow and blue regions, but it could be possible. The blue region is called the penumbral, where photoemission can occur due to incoming photons coming in at a severe angle. The shadow of these photoelectrons trickle into the penumbral region, but there should be no more photoemission by the yellow region. The green region is the stem of the system (the part that connects the photoemission cavity to

the B-Dot sensor). The transmission line for the axial set-up is modeled in this region parallel to the cathode.

A filtered 1 keV – 20 keV stainless-steel wire array x-ray input spectrum is incident upon an Au surface in the 10 mm or 1 mm cylindrical end photoemission driven cavity. The x-ray source is 500mm from the Au, and the pulse was modeled for the entire 30ns creating a time independent photoelectron spectrum. The x-ray time-pulse is a 3 ns FWHM pulse, as plotted below, with intensity plotted as a function of time.

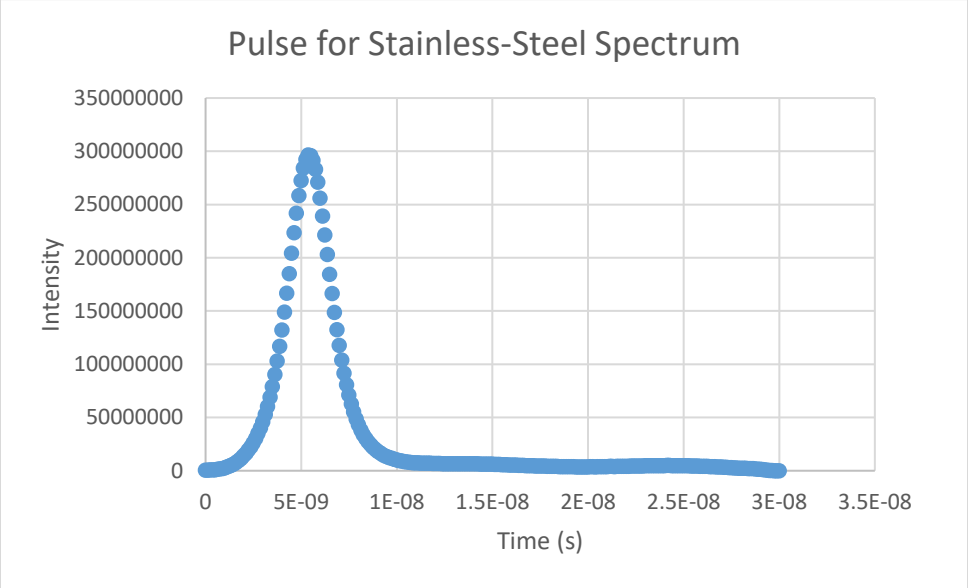

Figure 3.6 3 ns FWHM x-ray pulse for stainless-steel wire array experimentally measured from the Z-Machine at Sandia.

A filtered 1 keV – 32 keV silver spectrum from NIF x-ray input spectrum is incident upon an Au surface in the 10 mm or 1 mm cylindrical end photoemission driven cavity. The x-ray source is 500mm from the Au, and the pulse was modeled for the entire

30ns creating a time independent photoelectron spectrum. The x-ray time-pulse is a 1.5 ns FWHM pulse, as plotted below, with intensity plotted as a function of time.

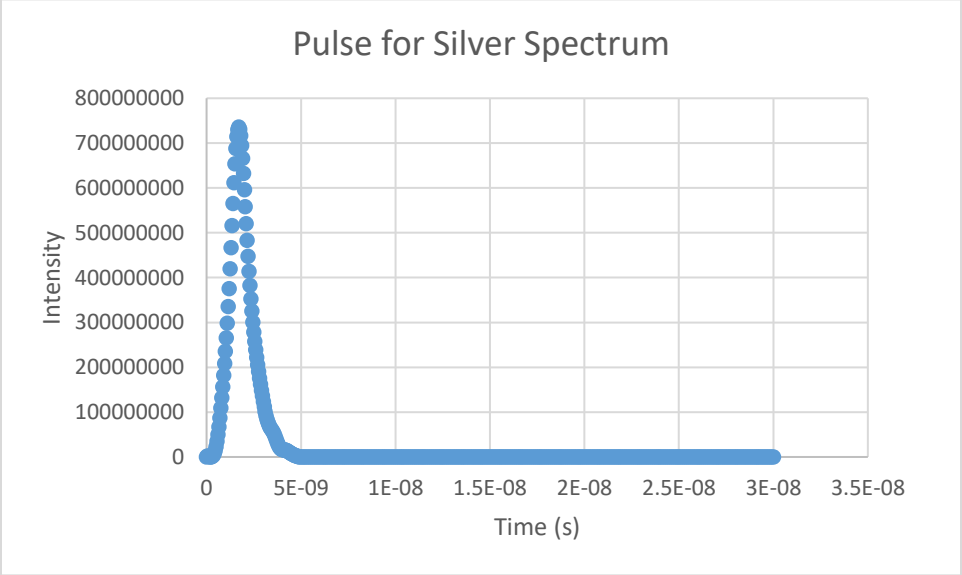

Figure 3.7 1.5 ns FWHM x-ray pulse for silver spectrum experimentally measure from the Z-Machine at Sandia.

3.2. MONTE CARLO PHOTON/ELECTRON TRANSPORT CODE

Below is the photoelectron output spectrum generated by the stochastic electron/photon transport code for Au. Surface 2 is the cathode with a higher photoelectron emission and Surface 1 is the anode with a lower photoelectron emission (Al with a thin Carbon coating). When comparing anode to cathode emission, we can essentially ignore the photoelectric emission of the anode because it is much lower than the cathode. For other diagnostics, such as a driven x-ray diode (XRD), we would have emission from both surfaces, as they are more comparable in energy.

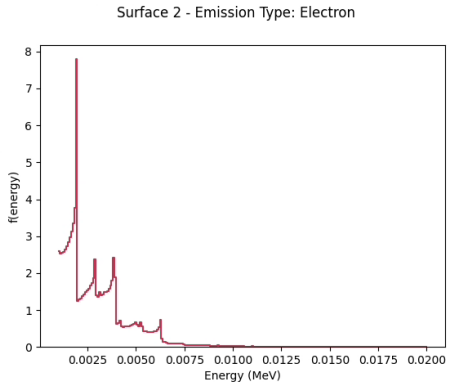

Figure. 3.8 Photoelectron output spectrum due to stainless-steel wire array x-ray irradiation in the stochastic photoelectron generator code in Au.

An important reason for choosing gold as our cathode is because gold emits many photoelectrons after irradiation. To show this, let's look at Ni's emission characteristics. Surface 1 is the same because it's still the Al with the Carbon filter. Surface two photoelectric emission is much different, as shown by the order of the y axis. Overplotting these spectra does not provide any new insight because there is such a large difference in emission intensities.

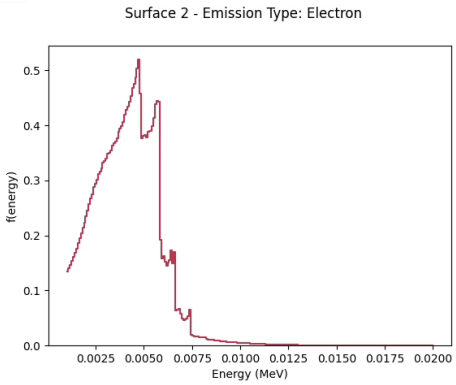

Figure 3.9 Photoelectron output spectrum due to stainless-steel wire array x-ray irradiation in the stochastic photoelectron generator code in Ni.

Notice how the emission for Ni peaks at around .5 at 5 keV. Au peaks around 8.0 at 2keV, so the peak emission for gold is much higher than Ni. Even at 5 keV, the emission for Au is just under 1, which is still double the emission for Ni. Figure 3.8 is a heat map in the theta direction for Ni and Au, which emphasizes the differences in electron emission on the two surfaces.

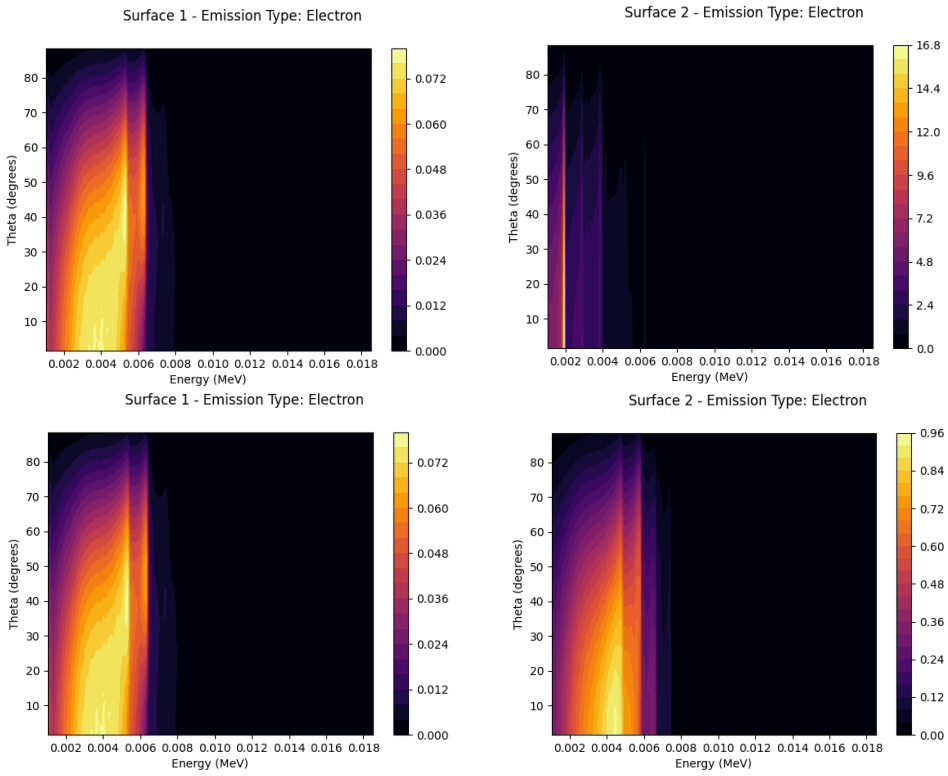

Figure 3.10 Heat map of photoelectron emission at different angles for Au (top) and Ni (bottom) for a stainless-steel wire array irradiation.

The graph for surface 1 is obviously the same because the anode is carbon coated Al, but the photoelectron emission is much stronger for Au than Ni, as seen by the color scale being vastly different.

Another input spectrum used in this work is a silver spectrum from the National Ignition Facility (NIF). This spectrum comes from experimental data collected at NIF, and it differs from the stainless-steel spectrum in many ways. The spectrum is not a z-pinch spectrum, and it comes from laser irradiation of a silver surface. The maximum energy photons are 20 keV for the stainless-steel spectrum, and the maximum energy photons are 32 keV for the silver spectrum. The output from the MC electron/photon code is shown in the Figure below. Notice how we can still assume that the cathode is the only surface that emits photoelectrons.

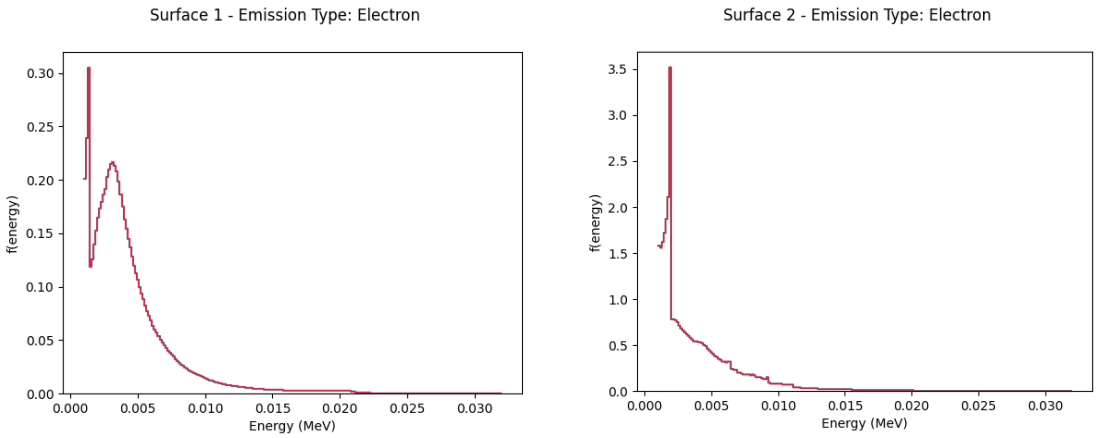

Figure 3.11 Photoelectron output spectrum due to x-ray irradiation from a silver source at NIF in the stochastic photoelectron generator code in Au.

When building the MC photon/electron code input file, a useful tool is aprepro. When using aprepro, one can define variables, perform calculations, and make changes to the geometry without having to change the each hard-coded instance of a variable. It is very useful and helps show where the numbers for the input file come from. Changing the

number of particles changes the accuracy of the simulation. The accuracy uncertainty in the data is proportional to $\sqrt{N}$, where N is the number of particles. We can map this convergence using a CDF to determine the minimum number of particles required to create an accurate photoelectron spectrum without reaching a point of diminishing returns for computational time. Since most of the emission is below 10 keV, it is more important to have high convergence at lower energies than at energies above 10 keV, where there are significantly fewer particles. We map this convergence by restarting our simulation many times. For example, if we modeled 1 billion histories in our simulation, we could restart our simulation ten times (at 100 million particles), output tally data, and dump our data into the next restart. This will help us determine when our simulation reaches a point of diminishing returns. The spectra generated above are for 2 billion particles, which is more than sufficient for our purposes. This will be proven in the results. Table 3.1 is a subsection of the MC photon/electron code output file for a stainless-steel input spectrum. The first column is energy bin in MeV, the 2nd, 4th, and 6th columns are photoelectric emission at a given angle, and the 3rd, 5th, and 7th columns are the uncertainty associated with the calculation, where lower is better.

Table 3.1 MC photon/electron code data showing uncertainty in each energy and theta bin.

ENERGY INTERVAL (MEV)						
2.000E-02 - 1.700E-02	8.07E-06	3	7.82E-06	3	7.72E-06	3
1.700E-02 - 1.692E-02	2.57E-05	10	1.77E-05	12	1.92E-05	12
1.692E-02 - 1.684E-02	2.89E-05	10	2.72E-05	10	2.28E-05	11
1.684E-02 - 1.676E-02	2.54E-05	10	2.59E-05	10	2.36E-05	10
1.676E-02 - 1.668E-02	3.14E-05	9	3.11E-05	9	2.56E-05	10
1.668E-02 - 1.660E-02	2.89E-05	10	3.01E-05	9	2.46E-05	10

3.3. EM PIC PLASMA PHYSICS CODE

After running the MC photon/electron code, calculations are performed for the full three-dimensional (3D) cylindrical cavity system. The photoelectron spectra from the AK gap are sent to the EM PIC code. There, calculations are performed by solving coupled Maxwell's equations with different fill gasses, gas pressures, and SCL "on and off" emission effects for the cylindrical cavity. The EM PIC code requires a time-pulse from experiment (30ns in this work), simulation time, and gas interaction cross sections data, which was provided by Tim Flanagan, R&D S&E in 1343. We also can change the geometry, distance from the detector, irradiated material, cavity gap size, inductance, and timestep. Calculations are performed and outputted for Bdl current (current induced in the B-Dot) and Edl current (the voltage across the gap). To create the EM PIC input file, you can again use aprepro. In the EM PIC code, aprepro allows you to code in variables and/or calculated values for points, boundary conditions, sidesets, and many more important characteristics of the geometry.

The EM PIC code is written in C++ and developed at SNL for electrostatic and electromagnetic simulations [18]. The EM PIC code accepts input files written using python wrappers. It relies heavily upon the Trilinos library and Kokkos, and together with MPI, can run on many different CPU's (central processing units) and GPU's (graphics processing units). Particles are tracked within and geometry, while fields are modeled within the mesh. As the particle location changes, the fields are updated based on the particles position and applies weights, and this process repeats for each particle at a given timestep. For a given geometry, one can define sidesets for each surface of the

geometry, and each sideset can have its own boundary condition. The following Figure shows the workflow of the EM PIC Code.

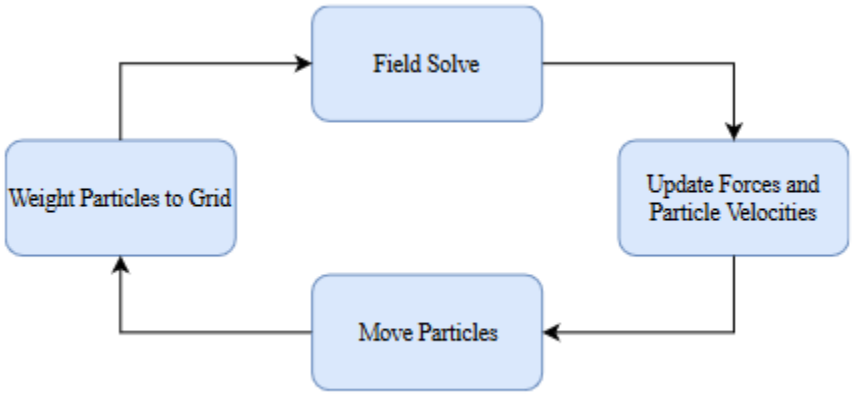

Figure 3.12 Workflow of the EM PIC code. Once a particle moves, the weight of the particle in the cell changes, which causes a change in the EM field. The fields are then updated, and the Lorentz force is calculated. The particle moves, and the process repeats [18].

The algorithm in the code numerically solves Klimontovich's equation for the time evolution of plasmas [18]. Maxwell's equations, where ρ is the charge density [19], govern the evolution of particles in an electromagnetic field, and the PIC code models the behavior of these particles in the presence of strong fields and plasmas. The code also creates "super particles", which are a collection of physical particles that reflect the behavior of a system, i.e., a plasma [18]. This reduces computation time. Some approximations are made within the code, but they are beyond the scope of this work, as we will focus on the code's output, rather than its algorithms. Different solver algorithms are available in the EM PIC code, including linear and non-linear solves, but for our purposes, a preconditioner with a defined maximum number of iterations is sufficient. To

improve stability of the simulation, one can adjust the Courant factor in the code, which increases your time-step, and prevents instabilities from causing a divergence in your system [20].

$$\nabla \vec{E} = \frac{\rho}{\varepsilon_0} \tag{18}$$

$$\nabla \vec{B} = 0 \tag{19}$$

$$\frac{\partial \vec{\mathrm{B}}}{\partial \mathrm{t}} = -\nabla \times \vec{\mathrm{E}} \tag{20}$$

$$\frac{\partial \mathrm{E}}{\partial \mathrm{t}} = \frac{1}{\mu_0 \varepsilon_0} \nabla \times \mathrm{B} - \frac{1}{\varepsilon_0} \vec{\mathrm{J}} \tag{21}$$

$$\mu_0 I = \int \vec{B}\, dl \tag{22}$$

Ampere's law (22) is how current is measure in the B-Dot. Bdl currents are computed for pressures ranging from vacuum to 1000 mTorr at 100 mTorr increments in Ne gas. Bdl currents are computed between vacuum and 500 mTorr for N_2 because we see the point of maximum electric discharge at pressures much lower than 1000 mTorr. SCL emission is toggled on/off in the simulation. Turning SCL emission on allows the Au surface to emit electrons if a surface electric field is present to allow electrons to accelerate into the gap. The presence of such an electric field is due to plasma generation in the cavity gap, and it continues to drive the maximum current through the B-Dot. A comparison of fill gasses is performed. The species of fill gas changes how much plasma is generated, as the energy required to ionize the fill gas changes. This work will focus on comparing N_2 and Ne fill gasses.

3.4. EM PIC TRANSMISSION LINE MODELING

The more efficient way to run this simulation, and the novel method described in this work, is modeling the cavity in two parts; the cavity and the stem (refer to the Introduction). After modeling the physics of the cavity, we can add a transmission line to the system. I first attempted to bring in the transmission line in radially, while adding a node set to the top and bottom curve of the side set on the outer radius of the cavity, as shown in Figure 3.13. This geometry does not model and mesh the B-Dot diagnostic itself but shows where transmission line was added. Boundary conditions are important for the circuit model, and they are set to a reflecting boundary condition.

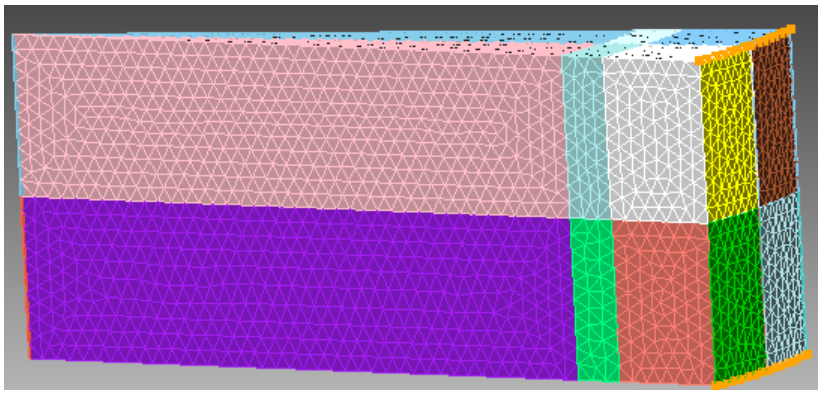

Figure 3.13 Cavity with node sets highlighted in orange. The top node set is the anode, the bottom is the cathode. To measure current at these locations, we add a transmission line in our code.

If we compare this Figure to Figure 3.4, we notice that we trimmed off the stem and the B-Dot sensor cavity. There are two ways to do this. One could build the entire system from pre-written code and trim off aspects of the system we do not wish to model,

or one could build it from scratch. I chose to build it from scratch because the prebuilt geometry meshes every volume in the geometry, and this is time consuming. Building the geometry from scratch allows us to obtain finer meshes quicker, as shown in Figure 3.14.

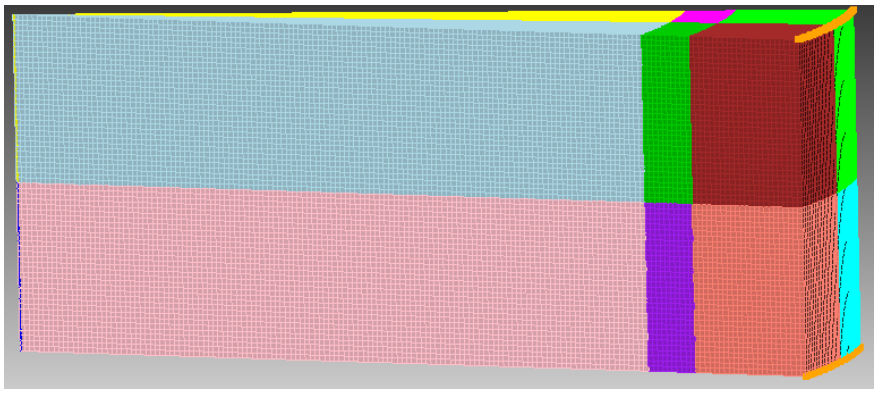

Figure 3.14 Simplified B-Dot geometry with finer meshes than the prebuilt geometry.

Sidesets were added for boundary surfaces of the simulation. There is a sideset for the top and bottom emitter respectively, the top and bottom penumbral regions respectively, the transmission line boundary, and each face of the wedge. These provide boundary conditions, which are all periodic except for the faces of the wedge, which are reflecting. Specifying boundary conditions properly is essential for modeling the geometry accurately.

The other way to model the transmission line is to bring it in axially. Instead of the transmission line anode and cathode ports being at the same distance from the center line of the cavity, the anode and cathode ports are at the same height as each other, and they are located at the bottom of the cavity. The transmission line is modeled at the

bottom of the stem that connects the cavity to the diagnostic, as shown in Figure 3.15. There is an extra set of volumes where the stem is located that was not modeled in the radial transmission line geometry. Notice how the meshing is slightly different as well. There must be 10 meshes across the transmission line, but the entire geometry does not need to be meshed as finely. Adding a stepped mesh function allows for a finely meshed transmission line region without causing the rest of the simulation to stall due to an overly fine mesh. Sidesets are defined in a very similar manner to the radial transmission line definitions, but the transmission line sideset is the surface between the cathode and the anode of the transmission line.

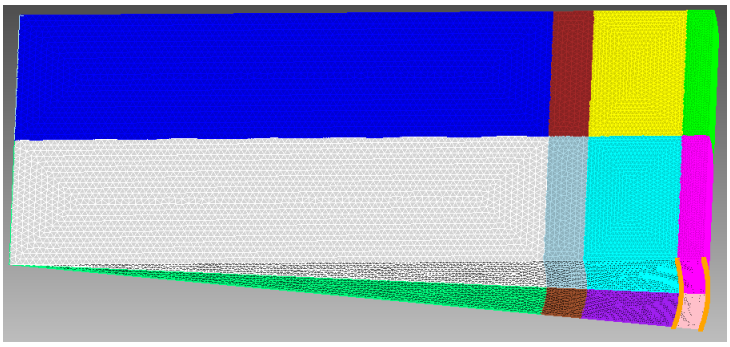

Figure 3.15 Photoemission cavity with node sets highlighted in orange where the axial transmission line is modeled. The inner node set is the cathode, the outer node set is the anode, 10 mm cavity gap.

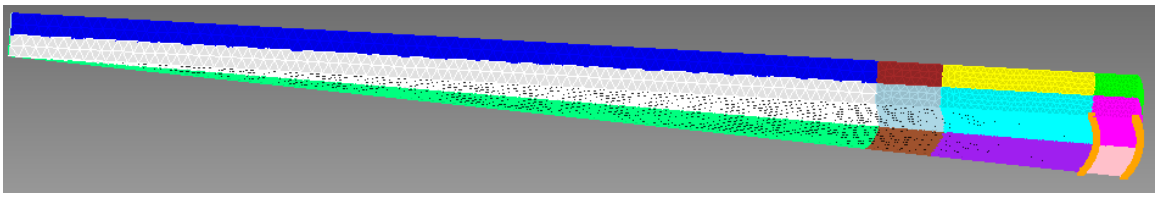

Figure 3.16 Photoemission cavity with node sets highlighted in orange where the axial transmission line is modeled. The inner node set is the cathode, the outer node set is the anode, 1 mm cavity gap.

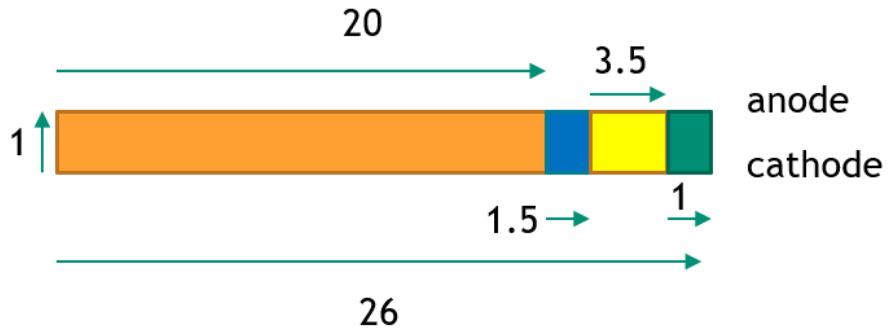

Figure 3.17 Sketch of the simplified 1 mm B-Dot photoemission cavity with dimensions in mm. The orange region is the photoemission region, with the top and bottom surfaces being the AK gap. All the distances are radii, and they are reflected about the far left of the sketch (like Figure 1.1). Photons come in from the top.

Inductances and capacitances that correspond to the resonant frequency ($\omega^2 = (LC)^{-1}$) were found in reference [4], and were added to the circuit model of the cavity. The values for L and C change with pressure, and they must be modeled accordingly. It is important to remember that the EM PIC code required values for L and C to be in L/meter, so we must divide each value by the length of the transmission line, which is coincidentally the height of the cavity.

Each sideset in the axial transmission line geometry is modeled as a perfect conductor except for the transmission line. This allows for current to flow easily through the circuit and through the cavity. The surfaces that are on the wedge (not the top and bottom surface) are given reflecting boundary conditions to complete the full cylinder of the geometry. The sideset where the transmission line cannot be defined as a perfect conductor because it has intrinsic capacitance and inductance per unit length, which prevents it from being a perfect conductor.

4. RESULTS

4.1. CONVERGENCE TESTING

Restarting the simulation and dumping the data for the next run provides data for smaller increments in the simulation and helps visualize the convergence of the system. Figures 18 and 19 show convergence of the MC photon/electron simulation with different number of particles for each surface (anode and cathode), with the obtained data being a due to restarts. Multiply the number on the legend by 1 million (.1 = 100,000, 20 = 20,000,000) for the number of particles. The input spectrum is still the stainless-steel wire array, and the material is gold. The difference in data for each bin for each simulation is compared to a simulation of six-billion particles, which is the most resolved simulation and assumed to be the true spectrum.

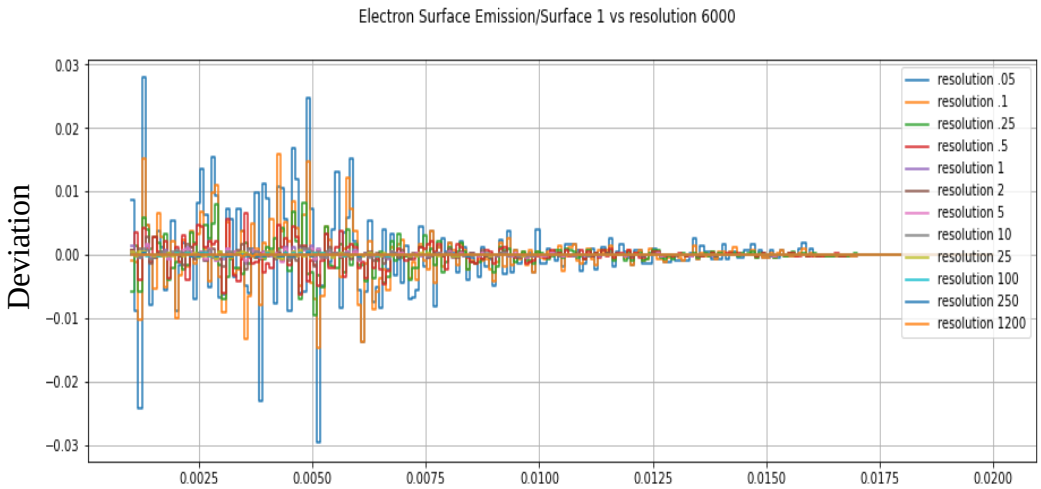

Figure 4.1 Convergence testing data from the MC photon/electron code for surface 1. This is a plot of the difference in the spectrum for different number of histories for the true spectrum of Au.

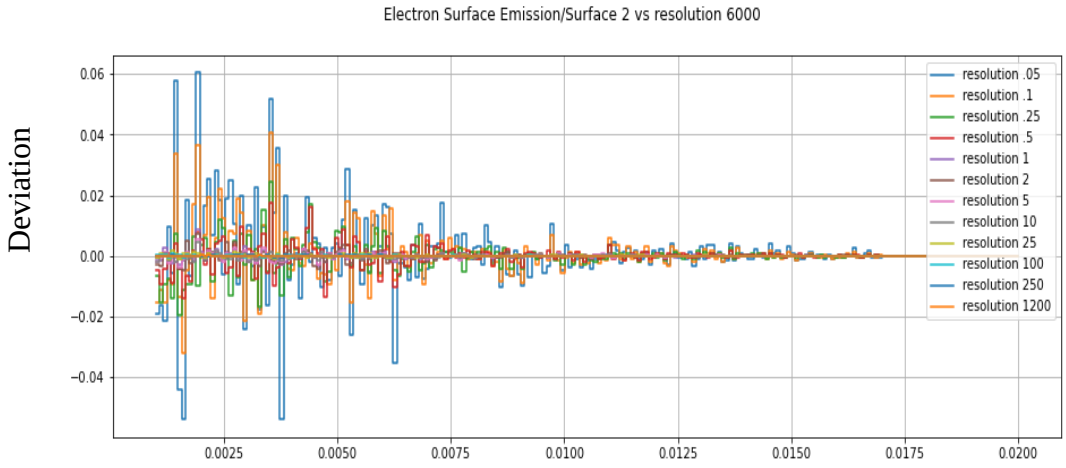

Figure 4.2 Convergence testing data from ITS for surface 2, a plot of the difference in the spectrum for different number of histories for the true spectrum of Au.

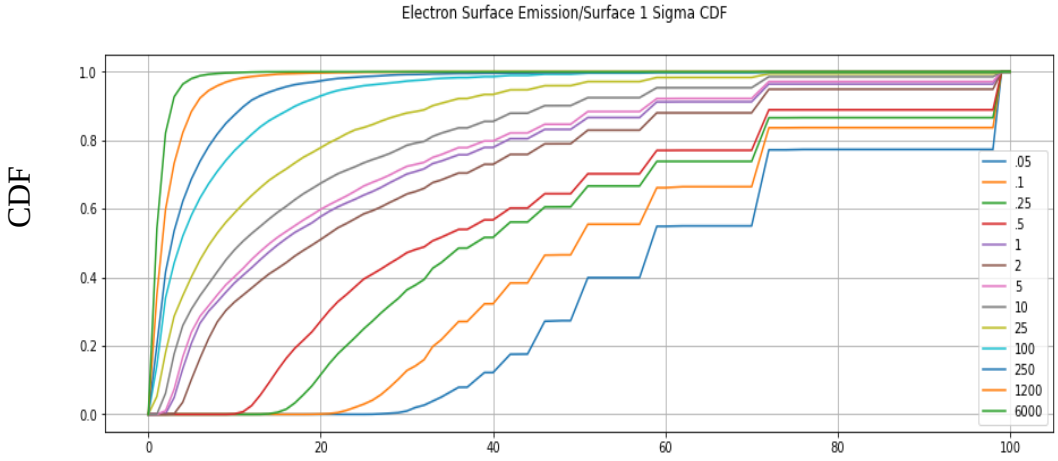

Figure 4.3 Convergence testing data from the MC electron/photon code for surface 1. The CDF shows the percent of energies with uncertainties below a given value.

Each energy bin has an uncertainty associated with the value obtained in the simulation, which decreases as number of particles increase. Figures 4.3 and 4.4 are for the same stainless-steel irradiation upon gold. The CDFs show what percentage of energy

bins fall below a given uncertainty for each surface. For example, Figure 4.3 has a simulation for 50,000 histories (.05 on the Figure). Fifty percent of the uncertainties are 40 or below. Any uncertainty below 10 is considered well resolved, and uncertainties increase as the energy bin increases.

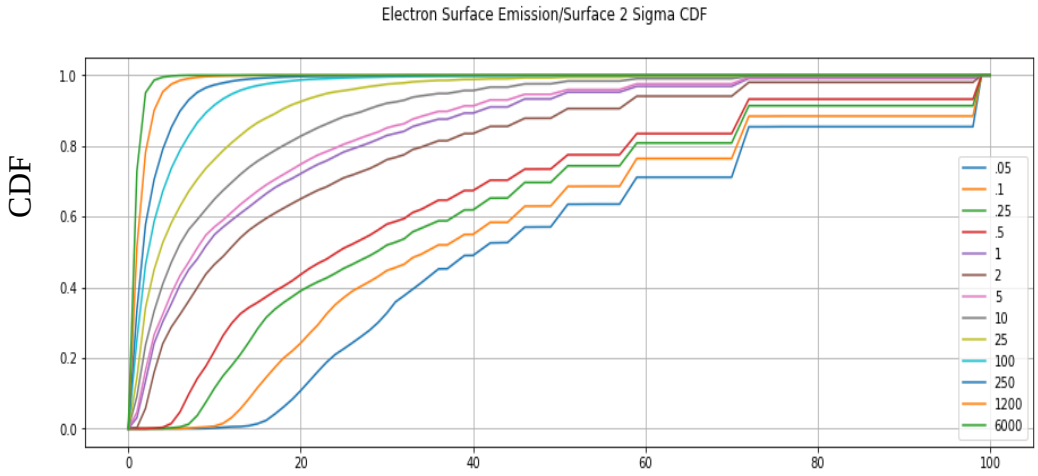

Figure 4.4 Convergence testing data from the MC electron/photon code for surface 2. The CDF shows the percent of energies with uncertainties below a given value.

4.2. BDL CURRENT OUTPUTS FOR FULL 3-D SIMULATION

The following plots were made in gnuplot [14]. .csv files from the simulations are created from the EM PIC runs, and gnuplot helps us visualize Bdl and Edl current outputs from the simulations. The x-axis is always time in nanoseconds. ParaView, or other similar plotting tools, are also a viable way to visualize fields, currents, electron densities, and other important physics of the simulation. When there is no fill gas, we can see that the Bdl currents are the same, even if we specify a fill gas in the code. This is not surprising, but this is a good sanity check to ensure the desired physics in your simulations are being modeled properly.

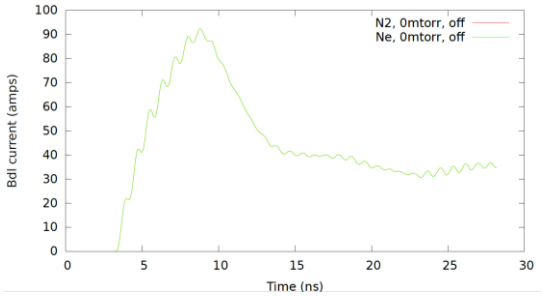

Figure 4.5 Bdl Current vs time, Au B-Dot full simulation, vacuum. This Figure compares telling the code Ne and N_2 fill gas at vacuum. Since there is no gas in the cavity at vacuum, these two outputs should be the same, and they are.

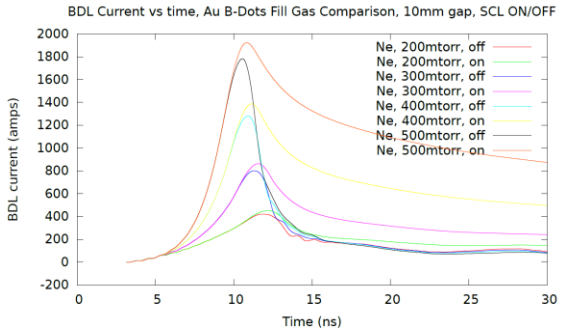

Figure. 4.6 Bdl Current vs time for Ne between 200 and 500 mTorr for a 10 mm Au B-Dot system, with SCL emission toggled on/off.

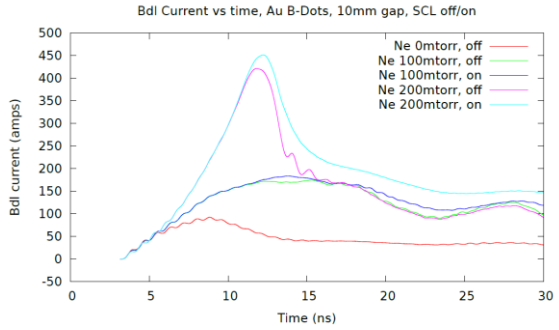

Figure 4.7 Bdl Current vs time for Ne between vacuum and 200 mTorr for a 10 mm Au B-Dot system, with SCL emission toggled on/off. Notice the LC cavity ringing in the tail of the pulse.

The time-pulse used in this experiment was provided by Tim Flanagan and was the same for both Ne and N_2 shots. Figure 4.5 shows the current output for gold between 200 and 500 mTorr with Ne fill gas. For SCL off cases, there are some oscillations in the current after the pulse. If the gap was at vacuum pressures, the oscillations come from the cavity acting like an LC circuit where we see ringing in the current. However, our minimum is 200 mTorr, so the cavity acts like an RLC circuit instead of an LC circuit and has less ringing than vacuum cases. More information on the physics and operations of the EM PIC code can be found in reference [18].

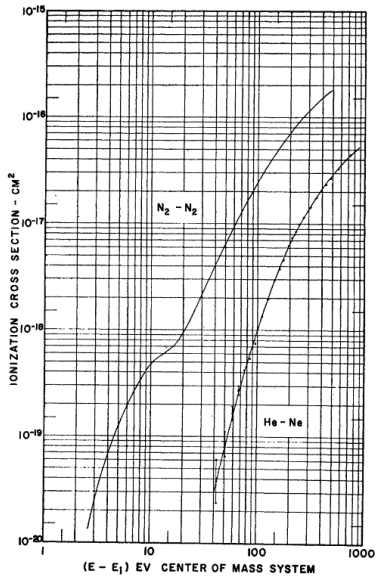

Figure 4.8 Gas ionization cross-sections for N_2 and Ne gas [21].

Unlike Ne, N_2 is diatomic; therefore, the physics of the cavity will be different. Figure 4.8 shows the gas ionization cross-section as a function of energy. N_2 has cross-sections that are orders of magnitude higher than Ne, so we expect to see higher peak

currents (more plasma in the cavity) and longer simulation times. The actual cross-section values are in the EM PIC code, and although the Figure is He ionization of N_2 and Ne, the differences in their respective cross-sections are apparent. The gas ionization cross-sections are also applicable to other ionization cross sections.

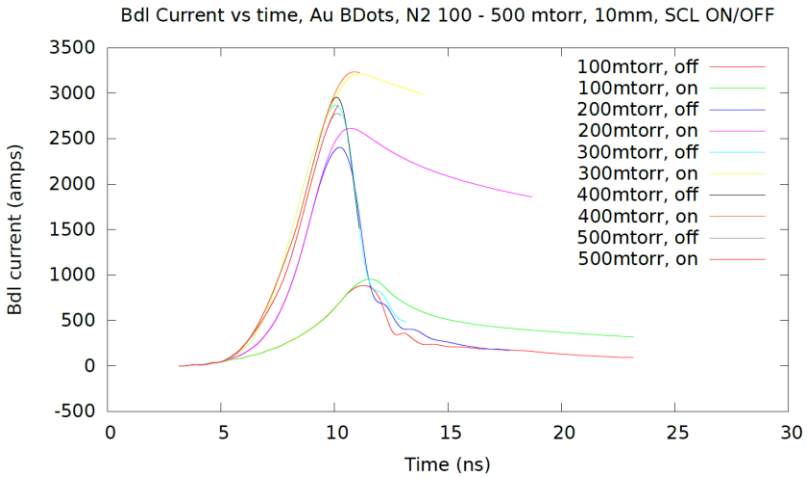

Figure 4.9 Bdl Current vs time for N_2 between 100 and 500 mTorr for a 10 mm Au B-Dot system, with SCL emission toggled on/off. These currents are much higher than Ne.

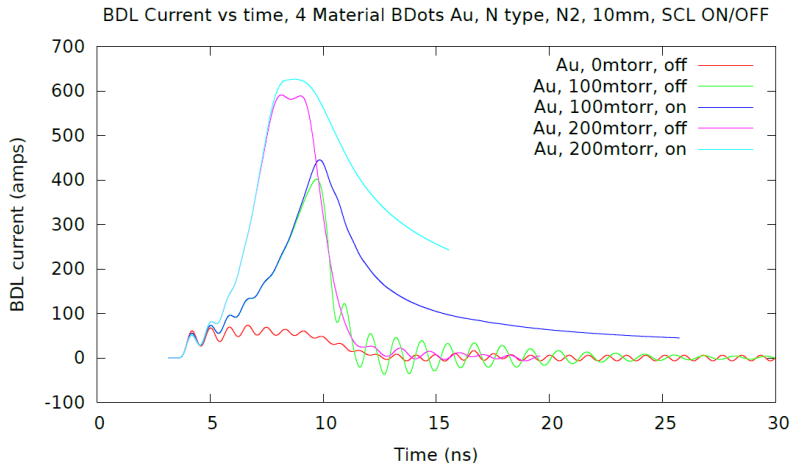

Figure 4.10 Bdl Current vs time for N_2 between vacuum and 200 mTorr for a 10 mm Au B-Dot system, with SCL emission toggled on/off. These currents are much higher than Ne.

This section will purely focus on comparing Ne to N_2. I will expand on the differences in SCL effects in the previous section. The following Figures are a direct comparison of Ne and N_2 fill gasses at pressures ranging from vacuum to 500Torr. At vacuum, there is no difference between SCL on and SCL off because there is no gas in the cavity, and therefore nothing to ionize. It is also independent from fill gas, which is confirmed by the simulation.

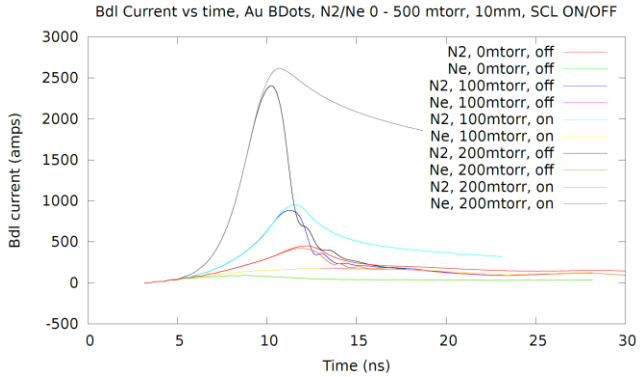

Figure 4.11 Direct comparison of Bdl Current vs time for Ne and N_2 fill gasses at low pressures.

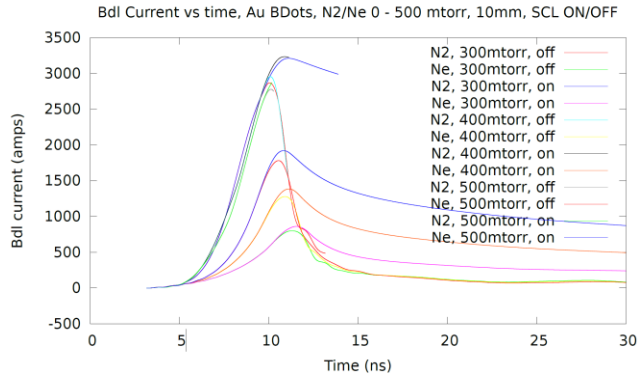

Figure 4.12 Direct comparison of Bdl Current vs time for Ne and N_2 fill gasses at high pressures.

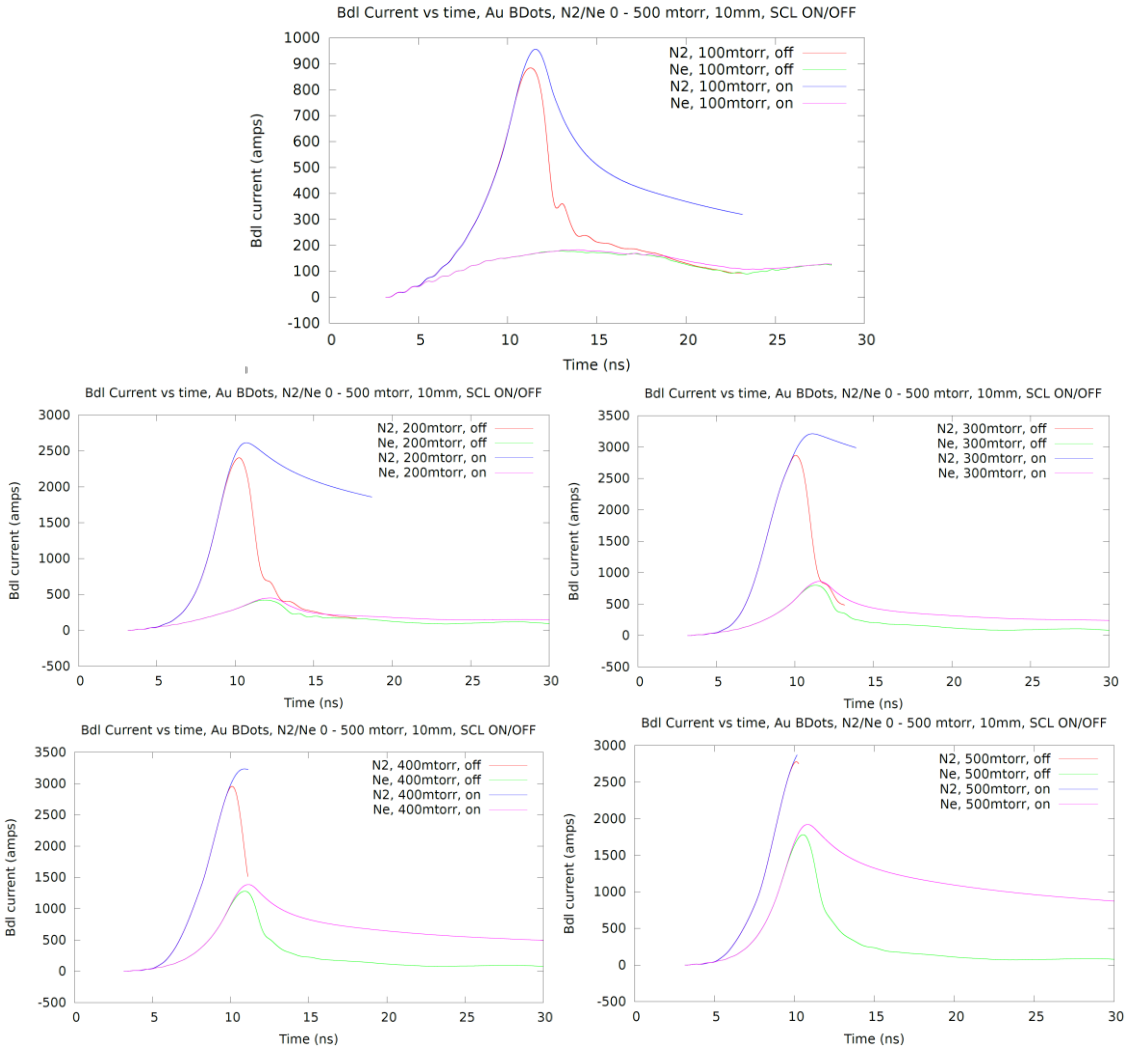

Figure 4.13 Direct comparison of Bdl Current vs time for Ne and N_2 fill gasses as a function of pressure, stainless-steel wire array.

Some of the simulations for N_2 timed out before being able to model the tail, but the key takeaway from these graphs is that N_2 emits many more electrons and generates a much higher current than Ne. However, it is interesting to note that N_2's curve peaks at 400 mTorr on (Figure 10). As shown in Table 2 and 3 in the appendix, we see that the difference between peak currents for each pressure of N_2 jumps quickly at low pressures,

but then does not increase linearly with pressure. Ne keeps increasing almost linearly as pressure increases, and slowly catches up to N_2's peak current. The reason for this is because the minimum voltage required for electric discharge is much lower for N_2 than for Ne. That is to say, the pressure that corresponds to the highest current generation is lower for N_2 than Ne. This is shown in Figure 2.2, the Paschen curve. The following Figures are a visualization of the differences in pressures at each pressure bin. For example, 2 on the x-axis corresponds to the jump between 100 and 200 mTorr, which increases by 1563A for N_2, SCL OFF.

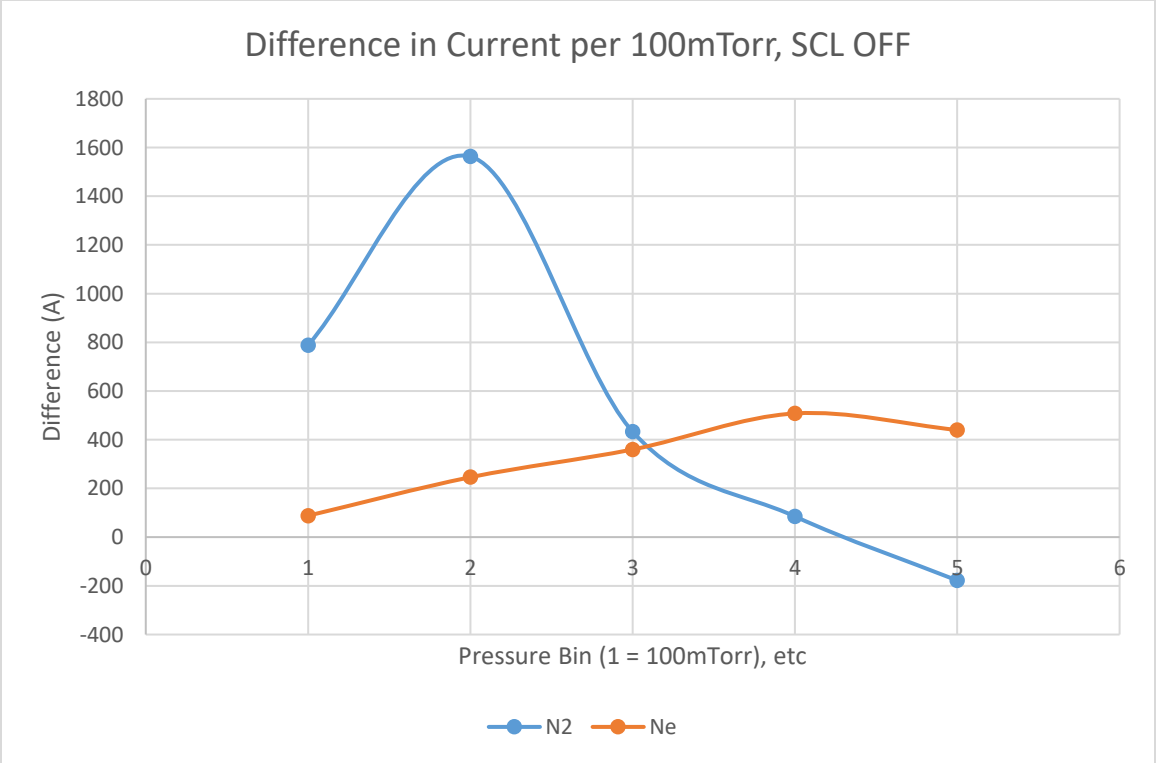

Figure 4.14 Difference in current vs pressure for 100 mTorr pressure bins in Ne and N_2 with SCL off.

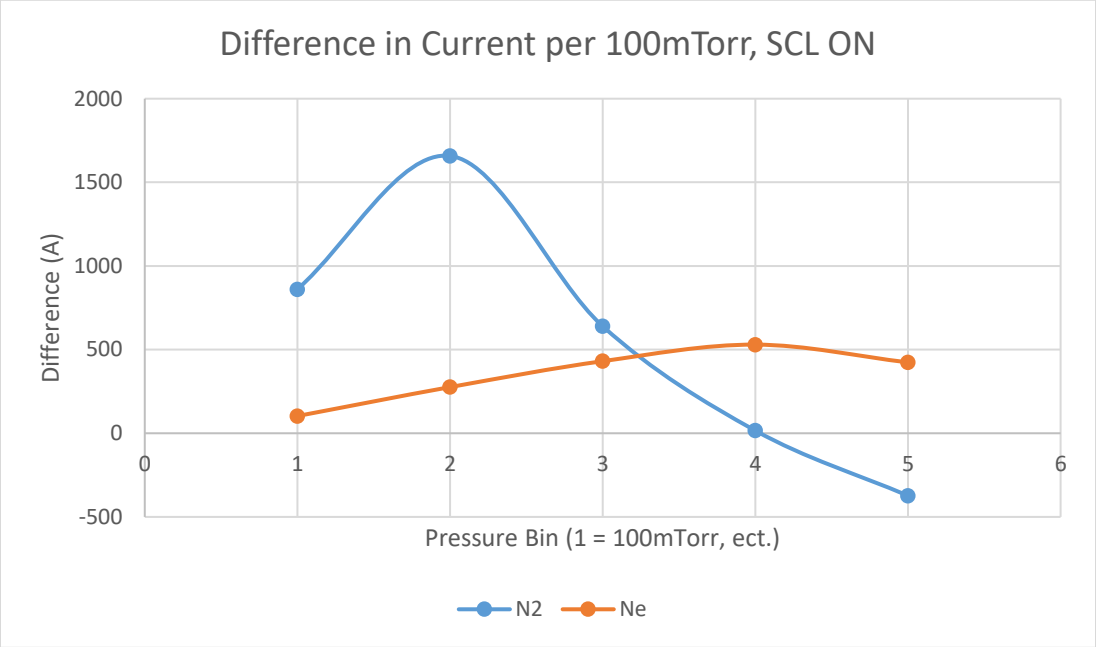

Figure 4.15 Difference in current vs pressure for 100 mTorr pressure bins in Ne and N_2 with SCL on.

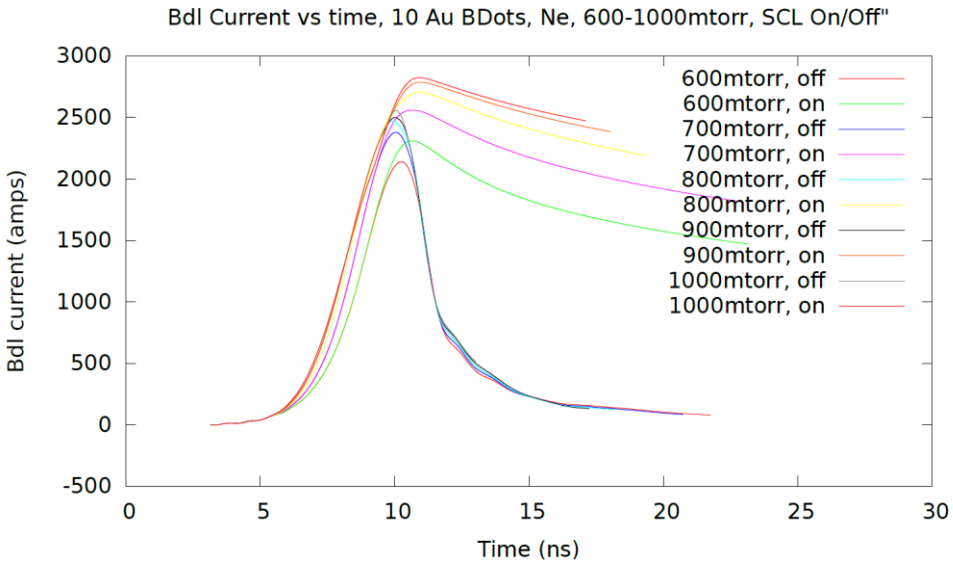

Figure 4.16 Bdl Current vs time for Ne between 600 and 1000 mTorr for a 10 mm Au B-Dot system, with SCL emission toggled on/off.

The simulation for the N_2 fill gas is much more computationally expensive than Ne because it has a higher ionization cross-section, which generates more photoelectrons to model. It is more useful to model N_2 because it is similar air, but since it is so computationally expensive, the simulations timeout before the tail can be properly modeled. It is trivial to model N_2 fill gas at pressures higher than 500 mTorr because we already know at what pressure the current peaks. For Ne, it is not so obvious. Below is the Bdl current output for a very high-pressure Ne gas filled B-Dot system.

As the pressure increases, the current increases for each case. However, the rate of increase decreases as a function of pressure. A similar chart to Figures 14 and 15 are shown below for Ne fill gasses between vacuum and 1Torr.

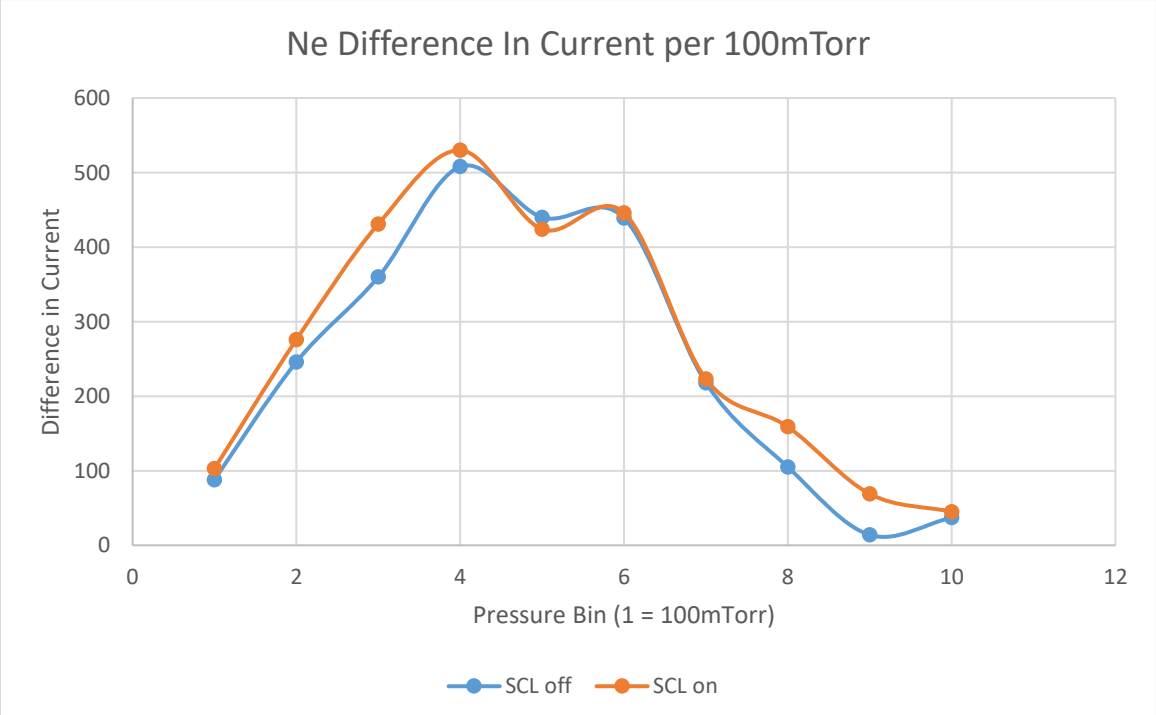

Figure 4.17 Difference in current vs pressure for 100 mTorr pressure bins in Ne. Notice how the current always increases as pressure increases (f(x) > 1 on the domain), but the rate of increase decreases substantially after 600 mTorr for SCL on/off.

Finally, notice the tail of the low-pressure pulses (Figures 4.7 and 4.9). At lower pressures, you can see clear oscillations. As noted in the background information, the cavity ringing can be explained as an LC circuit model.

4.3. SPACE-CHARGE LIMITED EMISSION

When SCL emission is turned on, we can see a much higher peak current as pressure increases, which is due to the neutralization of space charge electric fields in the gap by the plasma. SCL on allows electrons to be emitted from the surfaces long after the initial time-pulse. Without the presence of a plasma, the emitted electrons produce a space charge barrier that limits the amount of charge that can enter the gap. For example, let's look at the 400 mTorr graph from Figure 21. We see that the SCL on case has a higher peak current than the SCL off case, and the tail of the pulse drops off considerably (below 100A) after the initial irradiation pulse for the SCL off case because the maximum current is not driven to zero. For the Ne fill gas below 500 mTorr, peak current increases as pressure increases. When SCL emission is enabled, we see a significant amount of current in the circuit long after the initial time pulse. The tail from the SCL on case occurs because in the experiment the electric field from the ions in the plasma is driving the maximum amount of current possible until limited by space charge. When comparing the tails of the pulses, we see more oscillations in the SCL off case compared to the SCL on case. Toggling SCL on over-dampens (acts like a resistor in an RLC circuit) the oscillations, where the SCL on case behaves more like an LC circuit.

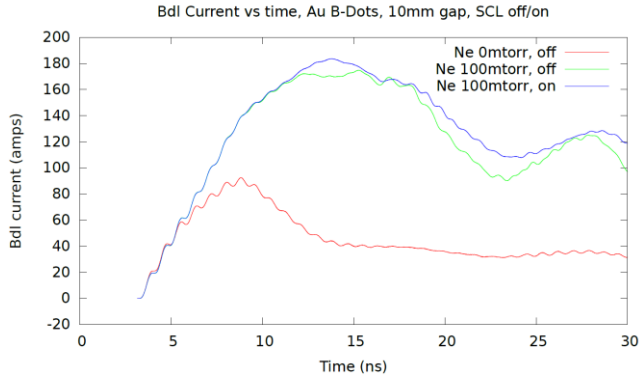

Figure 4.18 Bdl current vs time for Ne B-Dot simulations below 200 mTorr, SCL on/off, oscillatory.

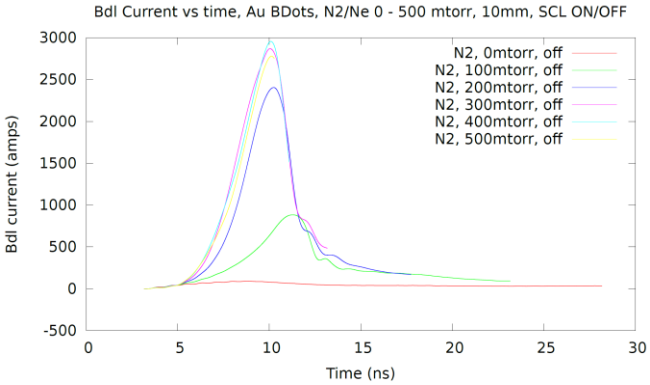

Figure 4.19 Bdl current vs time for 10 mm Au B-Dot with N_2 fill gas with SCL toggled off.

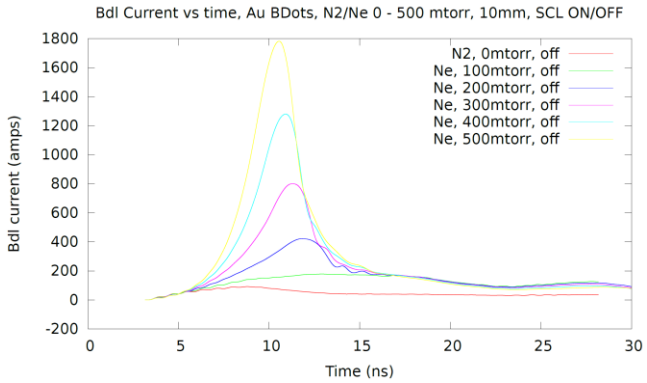

Figure 4.20 Bdl current vs time for 10 mm Au B-Dot with Ne fill gas with SCL toggled off.

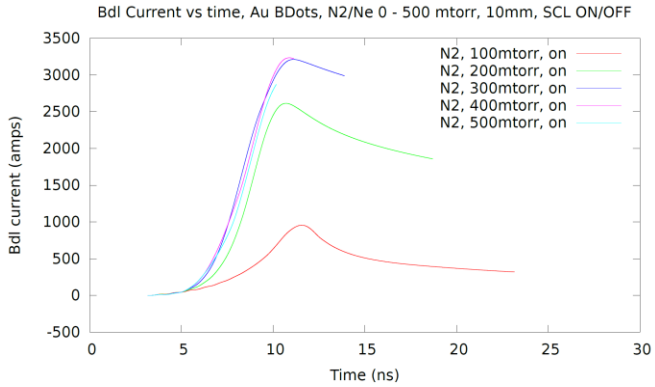

Figure 4.21 Bdl current vs time for 10 mm Au B-Dot with N_2 fill gas with SCL toggled on.

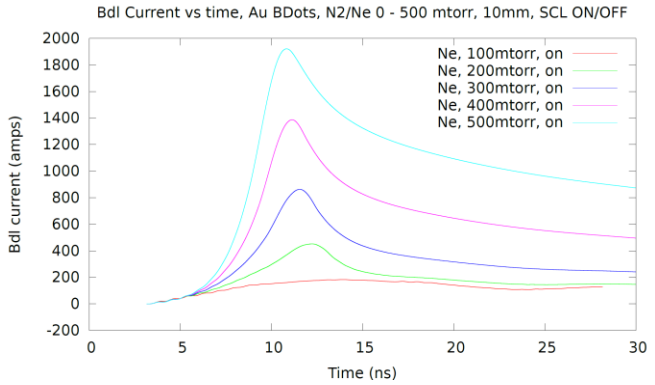

Figure 4.22 Bdl current vs time for 10 mm Au B-Dot with Ne fill gas with SCL toggled on.

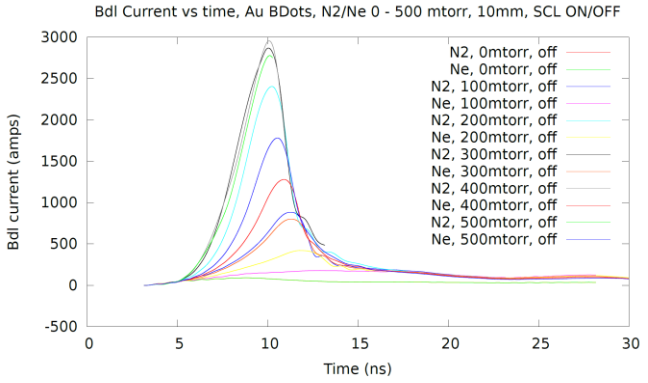

Figure 4.23 Bdl current vs time for 10 mm Au B-Dot, Ne and N_2 gas comparison, SCL off.

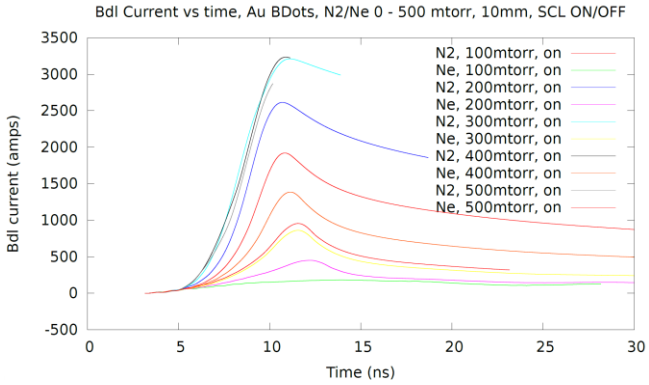

Figure 4.24 Bdl current vs time for 10 mm Au B-Dot, Ne and N_2 gas comparison, SCL on.

The SCL off case does not allow electrons to be emitted from the surfaces after the end of the x-ray pulse; therefore, the true expected current tail should lie somewhere between the two simulations for a given pressure, and the simulations provide a good upper and lower bound for the system. The SCL off case does not consider any plasma generation, while the SCL on case considers the maximum plasma generation in the system; therefore, the true expected tail should lie somewhere between the two simulations for a given pressure, and the simulations provide a good upper and lower bound for the system.

4.4. B-DOT OUTPUT FROM AXIAL TRANSMISSION LINE MODEL

Since the EM PIC code calculates the L and C values from the sideset associated with the transmission line, we can change the relative permittivity of the sideset to get our desired values for L and C. Below is a short proof of how we can do this. Transmission line length is 23mm, the distance from the cathode to the B-Dot in the 3D simulation.

$$c = \frac{1}{\sqrt{LC}} \tag{23}$$

$$c = \frac{1}{\sqrt{\mu_0 \varepsilon_0 \varepsilon_r}} \tag{24}$$

c is the speed of light, and ε_r is the relative permittivity. After some quick algebra, the relative permittivity is given by

$$\varepsilon_r = \frac{LC}{\mu_0 \varepsilon_0} \tag{25}$$

I noticed that changing the relative permittivity in the simulation only changes the capacitance, and one must change the relative permeability to change the inductance in the system. To do this, we can do a very similar derivation to find that

$$\mu_r = \frac{LC}{\mu_0 \varepsilon_0} \tag{26}$$

Table 4.1 Circuit model radial transmission line parameters

Inductance (nH)	.620
Capacitance (nF)	.058
Transmission line boundary (mm)	25
Cavity Height (mm)	10
Transmission Line Length (mm)	23

Table 4.1 gives values used in the EM PIC input file. Inductance and capacitance are calculated, and the distances are programmed in. The full 3D simulation only models a 15-degree wedge of the cavity, and I will do the same. However, not everything is

supported by the EM PIC code. The values for L and C were found in reference [4]. The code requires C and L per meter, and the values in the Table are not per meter. This is solved by multiplying these numbers by the height of the AK gap. My first attempt in creating the geometry oriented the cavity with symmetry in over the y-axis, and with the origin located in the center of the cavity. The following Figure shows my first attempt. Unfortunately, this would not work with how the EM PIC code is set up, because the geometry must have symmetry in the XZ plane, not the YZ plane. The code is not set up to handle anything else. Also, the top or bottom of the cavity's inner radius must be at the origin, and the mesh must be a tet-mesh.

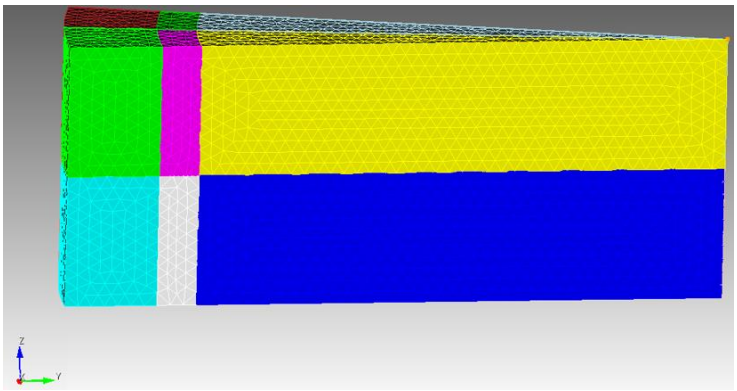

Figure 4.25 First attempt at creating the cavity. The x-axis is oriented into the page, and the y-axis moves "left to right". Notice the origin located at the orange dot. The mesh is a tet-mesh.

I fixed the errors above to comply with the way the code was built by creating a geometry with XZ symmetry and moving the geometry down half the height of the cavity. I arbitrarily chose the origin at the top of the cavity (on the anode) because that is

what was chosen by the full 3D simulation. The following Figure shows the final geometry with the proper parameters. Important code blocks can be found in the appendix.

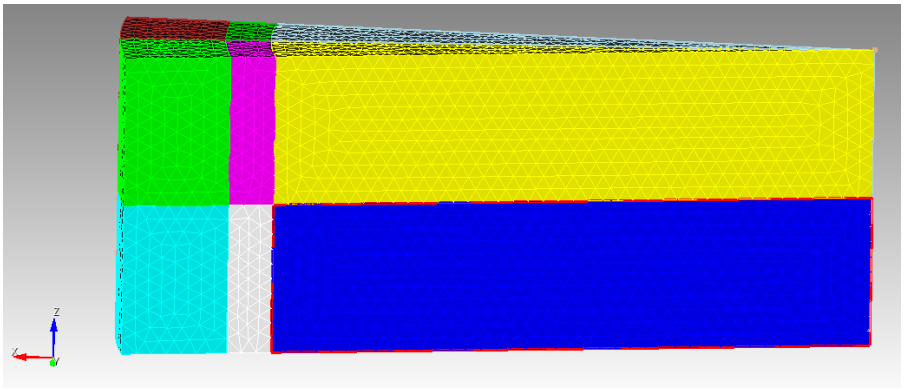

Figure 4.26 Final geometry of the cavity. The x-axis moves “left to right”, and the y-axis is oriented into the page. Notice the origin located at the orange dot. The mesh is a tet-mesh.

For the axial transmission line, each length of the circuit has its own inductance and capacitance values. These values were calculated using the ideal inductance and capacitance equations for a transmission line, as shown in equations 22 and 23, where b is the outer radius, and a is the inner radius. Table 4.2 shows the calculated LC values for each segment along the B-Dot circuit.

$$C = \frac{2\pi\varepsilon_0\varepsilon_r}{ln\left(\frac{b}{a}\right)} \tag{27}$$

$$L = \frac{\mu_0\mu_r}{2\pi}\ln\left(\frac{b}{a}\right) \tag{28}$$

$$R_{Sideset} = \sqrt{L/C} \tag{29}$$

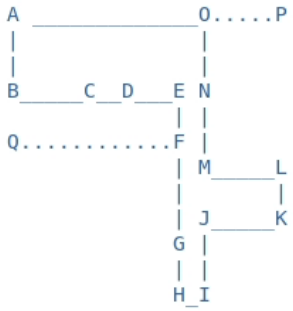

Figure 4.27 B-Dot transmission line segments, each section correlates with an LC value in Table 4.2.

Table 4.2 L and C per unit length of each section of the transmission line circuit. G_l is conductivity, and the default is 0.0.

#Length	num_cells	C_l	L_l	G_l
0.002	20.0	5.910195817843425e-11	1.882594232655415e-07	0.0
0.011	110.0	5.910195817843425e-11	1.882594232655415e-07	0.0
0.01	100.0	6.889189348252632e-12	1.6150667368952925e-06	0.0
0.005	50.0	1.1705623268286148e-10	9.505261108719454e-08	0.0
0.002	20.0	1.1705623268286148e-10	9.505261108719454e-08	0.0

As a proof of concept, I ran a B-Dot Cold Test with the new geometry, with the transmission line on the edge of the cavity. This simulation is quicker than the cases with fill gas and SCL emission effects, and it helped me with debugging. The Cold Test is driven by a beam of electrons with constant energy instead of the photon spectrum generated by the MC photon/electron code. The sidesets were changed to have periodic or reflecting boundary conditions, except for the transmission line, which has an absorbing boundary condition. Below is the geometry of the diagnostics from ParaView.

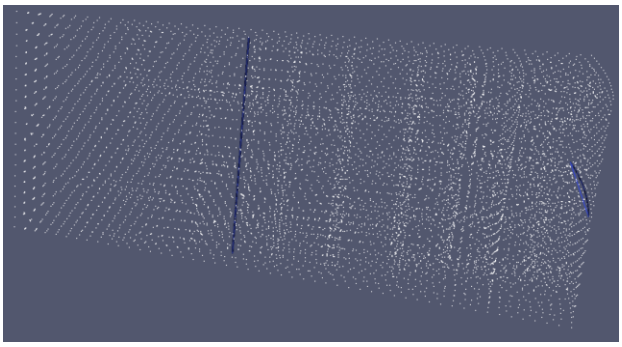

Figure 4.28 Visualization of the diagnostics in the cavity. The vertical blue line is the Edl diagnostic, the curved horizontal blue line is the Bdl circle current diagnostic at the transmission line.

4.5. TRANSMISSION LINE MODELING

The results in the previous sections describe a geometry where the cavity height is 10 mm. However, 10 mm cavities are highly space-charge limited, and the transmission line may not be the dominant physics of that geometry. To prove that the modeled transmission line does in fact affect the system, a geometry with a 1 mm cavity gap was modeled, with transmission lines appearing in the same places as the 10 mm cavities. The following Figure shows the full geometry of a 1 mm gap B-Dot system.

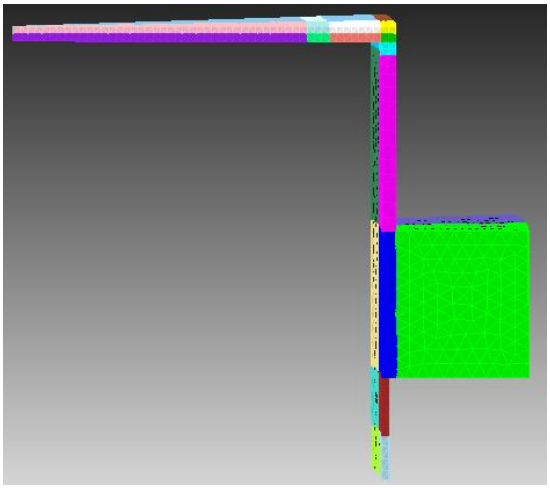

Figure 4.29 Full geometry of 1 mm B-Dot. The A/K gap is 1 mm instead of 10 mm.

Another geometry used on the Z machine is an LB-Dot, where L stands for inductance. These geometries have higher inductance values in the circuit, and greatly reduce the current output. These geometries have much more ringing in the cavity after the initial x-ray pulse, and the oscillations are more well defined than regular B-Dots. The geometry is modeled in Cubit and is shown below.

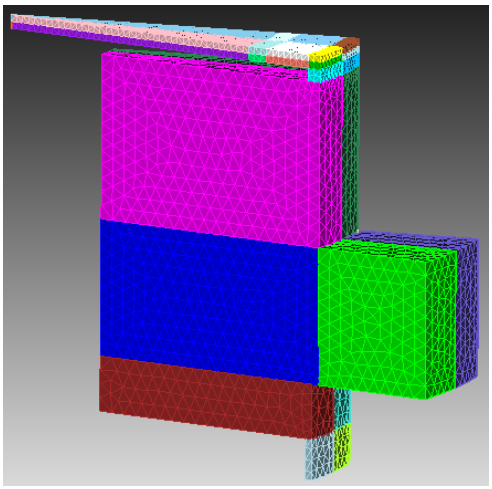

Figure 4.30 Full geometry of 1 mm LB-Dot. The A/K gap is 1 mm, and the block below the cavity increases the inductance of the entire system, which reduces the peak current output.

The low-pressure current outputs for the full geometries are shown below for the SCL on and off cases for a stainless-steel wire array input spectrum. As expected, peak current increases as pressure increases. Modeling SCL effects dampens the tail of the circuit. This is apparent in the SCL on case in the LB-Dot graph. For SCL off, we see some oscillations before eventually flattening out, but SCL on cases do not oscillate.

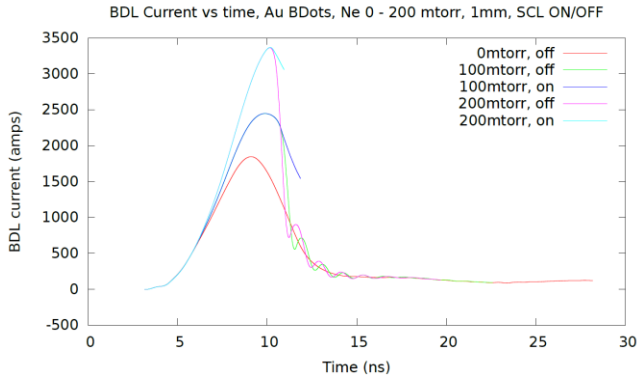

Figure 4.31 Bdl current vs time for a 1 mm B-Dot for pressures between 0 and 200 mTorr, full geometry, stainless-steel source.

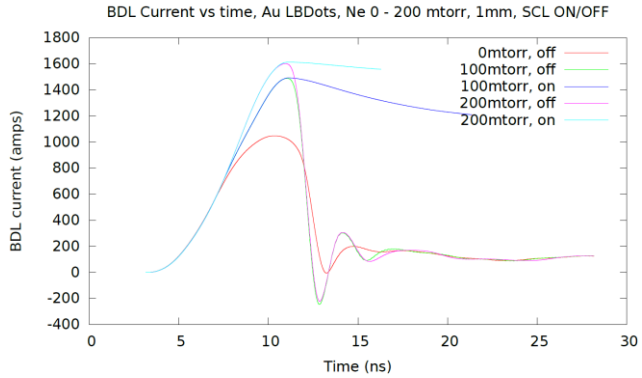

Figure 4.32 Bdl current vs time for a 1 mm LB-Dot for pressures between 0 and 200 mTorr, full geometry, stainless-steel source.

When modeling the transmission line, the geometry for B-Dot and LB-Dot cases are the same, as shown below. The inductance and capacitance parameters of the transmission line can be changed in the input deck, allowing us to use the same geometry for both cases. This is another reason why modeling the circuit as a transmission line simplifies these experiments. The mesh is also finer. I used a stepped mesh that is between 2 and 5 times finer than the original mesh, which should improve the accuracy of the simulation.

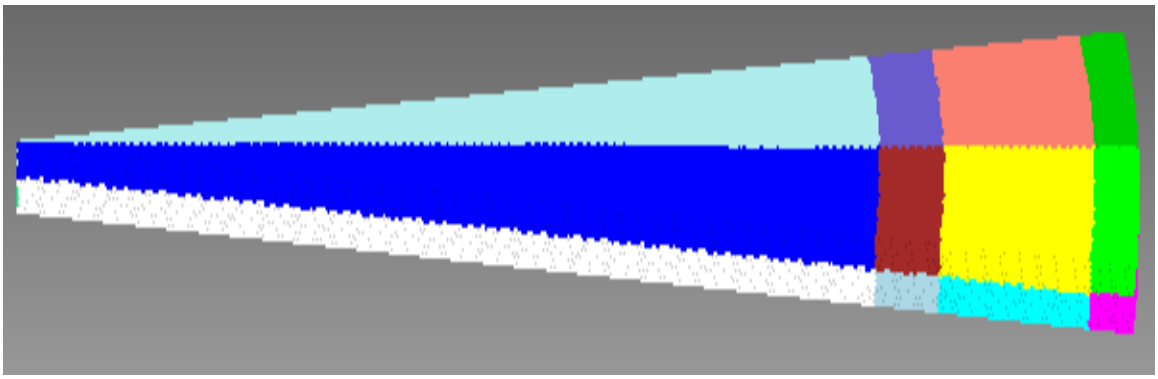

Figure 4.33 1 mm B-Dot and LB-Dot photoemission cavity. If modeling the transmission line, the rest of the geometry can be ignored, just like the 10 mm case.

In the circuit block, the voltage is set to zero because the A/K gap is not driven. To do this, the source resistance must be set to a very low value. In 10 mm AK gap simulations, the resistance value does not impact the current output because the transmission line is not the dominant physics. In 1 mm simulations, the resistance value should be as close to zero as possible within the tolerance of the code. I chose $R = 10^{-14}$ ohms.

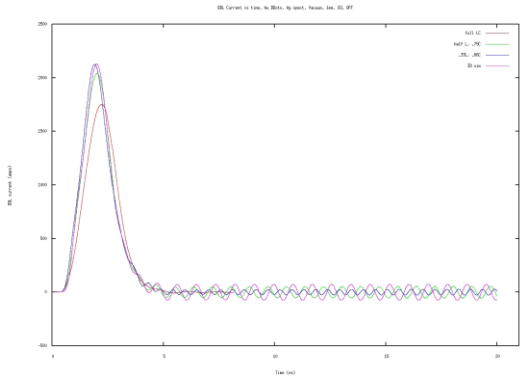

Figure 4.34 Bdl current vs time for a 1 mm vacuum B-Dot with the circuit modeled as an axial transmission line with different inductance values compared to the full simulation, silver source.

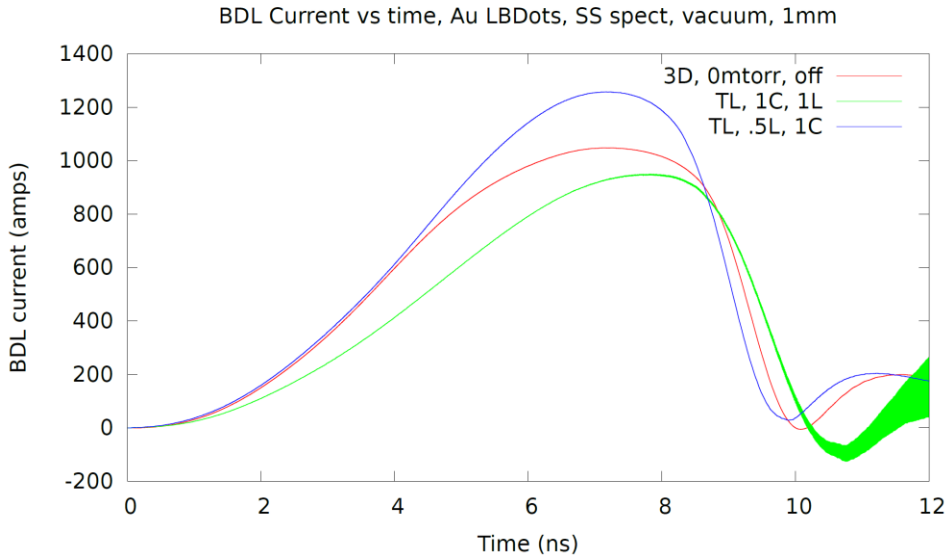

Figure 4.35 Bdl current vs time for a 1 mm vacuum LB-Dot with the circuit modeled as an axial transmission line compared to the full simulation, silver source.

There is a sensitivity parameter built into the workflow for these types of simulations. The expected sensor cavity radius is 35 mm, but you can increase the sensitivity by changing this radius to 30.5 mm. This does not affect our geometry in the transmission line simulation, but it does change the values for L and C. Although the cavity geometry looks the same, the LC parameters calculated in the transmission line differ, which will lead to slightly different current outputs. A Figure comparing the two sensitivities is shown below, where N is 35 mm (normal), and V is 30.5 mm (very reduced). L and C values were calculated for each sensitivity, but the output is not very different. The V type output has a slightly higher peak current and a slightly quicker rise time, but they are essentially the same graph. From here on out, all outputs will be for V type geometries.

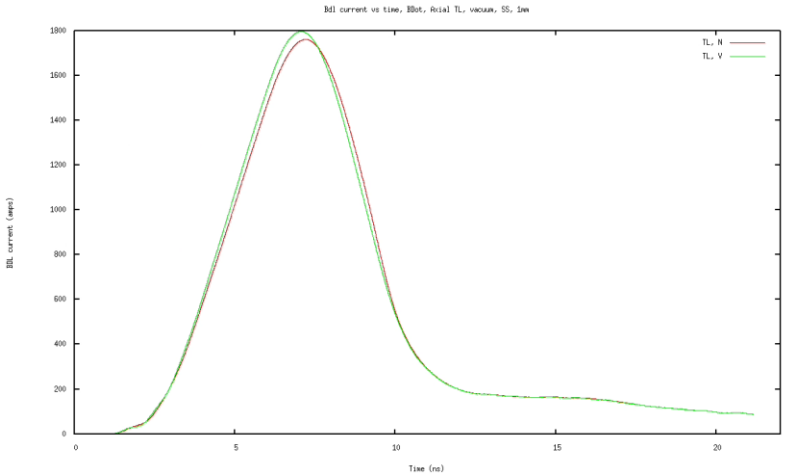

Figure 4.36 Bdl current vs time comparing current outputs for normal and very reduced sensitivity. Notice how the tail matches perfectly for both geometries.

From the silver source B-Dot simulation, we see that the calculated value for L does not produce the peak currents we expect, it is too low. Changing the inductance to half the calculated value provides an accurate picture of photoelectric emission in the cavity. The oscillation periods and magnitudes in the tail of the pulse for the cases where the L and C are changed are slightly different than the full 3D simulation, but the peak current is more accurate. The oscillation frequency, ω, is the square root of 1/LC, so changing L and/or C greatly changes the characteristics of the tail. As expected, when the quantity LC is reduced, the period increases, as shown by the silver source B-Dot current output. The LB-Dot configuration should have definite oscillations, as the inductance is much higher than the B-Dot configuration, and the capacitance is much lower. However, the simulation diverges around 10ns in the original inductance case, so seeing these larger oscillations is not feasible using the transmission line.

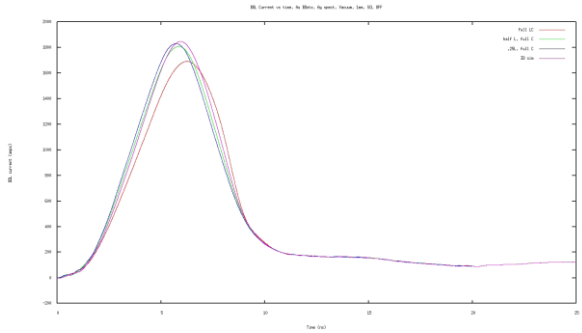

Figure 4.37 Bdl current vs time for a 1 mm vacuum B-Dot with the circuit modeled as an axial transmission line with different inductance values compared to the full simulation, stainless-steel source.

The 10 mm cases are trickier to work with. In 1mm cases, changing the inductances and capacitances in the transmission line changes the Bdl current output of the cavity. However, 10 mm cavities are highly space-charge limited, and the dominant physics is not captured by the LC circuit. No matter what values are used for LC, the Bdl current output does not change, as shown in the Figures below for both a silver and stainless-steel spectrum. When the resistance (equation 23) is changed to a large value (1 ohm), there is no change in the Bdl current output. The resistance should be close to zero (I'm using 10^{-14} ohms) because the cavity is not driven.

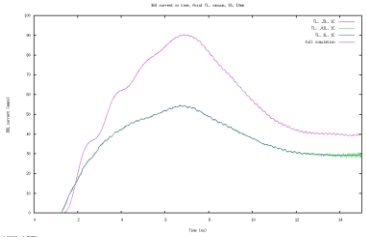

Figure 4.38 Bdl current vs time for a 10 mm vacuum B-Dot with the circuit modeled as an axial transmission line with different inductance values compared to the full simulation, stainless-steel source.

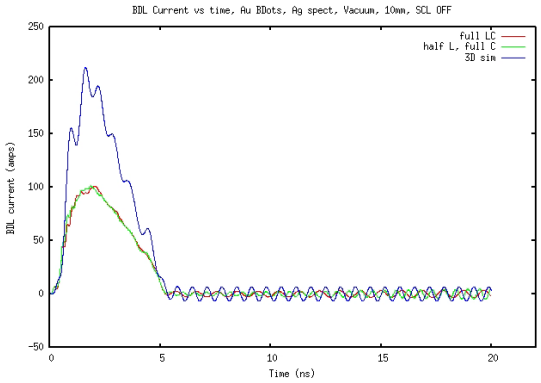

Figure 4.39 Bdl current vs time for a 10 mm vacuum B-Dot with the circuit modeled as an axial transmission line with different inductance values compared to the full simulation, silver source.

1 mm gap simulations are more sensitive to LC transmission line effects. However, it seems that the simulations are much more accurate when the capacitance is held at the expected value, while the inductance is cut in half, as shown in the graph for 1 mm stainless steel with different varied LC values. Table 4.3 shows the LC values that will be used when the inductance is cut in half. However, we can use the oscillation period from the Ag simulations to calculate L and C per unit length. These values were calculated in the 1 mmV vacuum case, and then the values were used for simulations with a fill gas.

Table 4.3 L and C values for the axial transmission line. Inductance values are half of the calculated values, which yields more accurate results for Bdl current.

#Length	num_cells	C_l	L_l	G_l
0.002	20.0	5.910195817843425e-11	9.412971163277076e-08	0.0
0.011	110.0	5.910195817843425e-11	9.412971163277076e-08	0.0
0.01	100.0	6.889189348252632e-12	9.54484122635e-07	0.0
0.005	50.0	1.1705623268286148e-10	4.752630554359727e-08	0.0
0.002	20.0	1.1705623268286148e-10	4.752630554359727e-08	0.0

When calculating the L and C values from the coaxial cable equations, we notice that the current peaks, pulse shape, and oscillations do not match a full simulation. This is an issue, because these calculated values should be similar to the expected intrinsic LC values in the coaxial cable. However, when we cut the inductance in half, we see a much more accurate picture of current outputs. This is because the inductance is being modeled twice as the EM pulse transmits through the circuit. If you look at the geometry of the B-Dot return circuit, the current bounces back, and the inductance is modeled twice. The voltage in the inductor has the form, $V = L\frac{dI}{dt}$, where the voltage in the capacitor has the form $V = CQ$. Because of the $\frac{dI}{dt}$ dependance of the inductor, it is more sensitive to changes than the capacitor is. Table 4.4 shows the analytically fitted LC values per unit length.

Table 4.4 L and C values for the axial transmission line. Inductances and capacitances were fit to the Ag 1 mmV oscillations analytically, which yields more accurate results for Bdl current.

#Length	num_cells	C_l	L_l	G_l
0.002	20	1.003492148e-10	6.852643008e-08	0.0
0.011	110	1.003492148e-10	6.852643008e-08	0.0
0.01	100	1.979256108e-11	3.474322207e-07	0.0
0.005	50	1.987497774e-10	3.459915044e-08	0.0
0.002	20	1.987497774e-10	3.459915044e-08	0.0

However, cutting the inductance in half still does not produces perfectly similar results. A big issue is seen in the silver spectrum current outputs, where the oscillations in

the tail do not match in the full and transmission line simulations. The oscillation period and amplitudes are not the same. From the full vacuum simulation, we can calculate the expected value for inductance, and use that value for higher pressure simulations. The observed inductance differs from the calculated transmission line inductance because the simulation is not modeling a perfect coaxial cable, and these slight differences in calculations leads to different oscillation periods and peak currents. Although the stainless-steel current output plots do not have as many oscillations, we can still use the observed transmission line values to predict the current output for cases when a fill gas is added. The drawback to this method is that a full geometry vacuum run is required to calculate L, which can be inconvenient. However, vacuum simulations can be run in with fine meshes in less than two hours on just a few nodes.

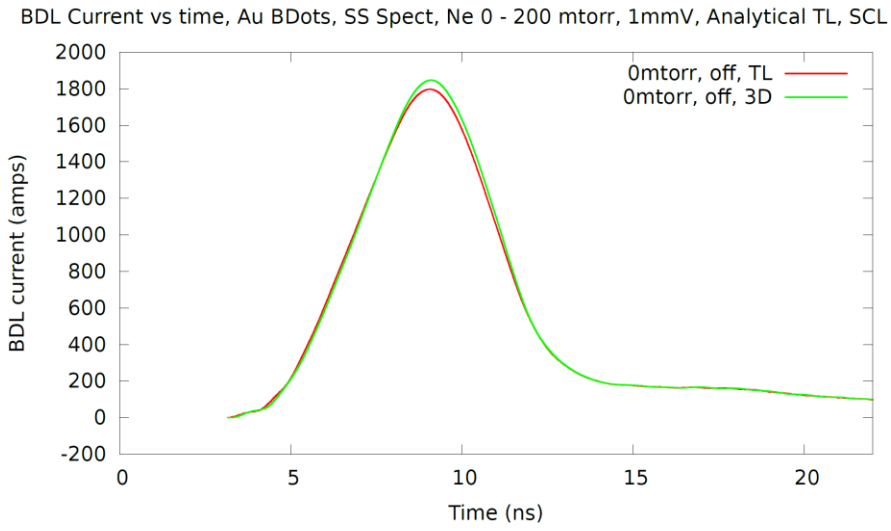

Figure 4.40 Bdl current vs time for a 1 mm B-Dot with the circuit modeled as an axial transmission line at vacuum. LC values come from an analytical fit of the silver spectrum oscillations.

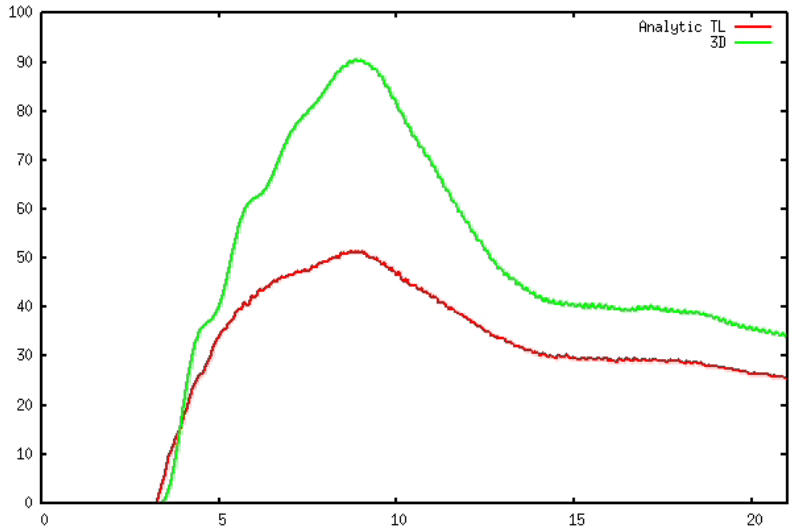

Figure 4.41 Bdl current vs time for a 10 mm B-Dot with the circuit modeled as an axial transmission line at vacuum. LC values come from an analytical fit of the silver spectrum oscillations.

A Ne fill gas at various pressures was added to the 1 mm B-Dot cavity, and the current was plotted. 3D refers to the full simulation, where the B-Dot diagnostic was modeled. TL stands for transmission line, and those simulations do not model the B-Dot, but replace it with a transmission line, with LC values from Table 4.3.

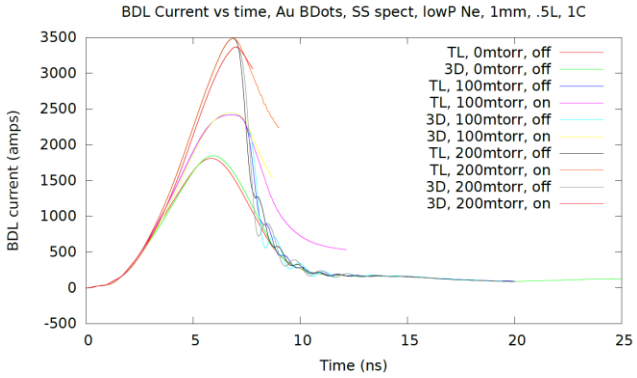

Figure 4.42 Bdl current vs time for a 1 mm B-Dot with the circuit modeled as an axial transmission line with low-pressures of Ne fill gas. SCL ON/OFF.

TL refers to B-Dot simulations where only the cavity is modeled, and 3D refers to simulations where the stem, B-Dot, and cavity are modeled. As shown in the Figure, the peak currents from the TL and 3D simulations differ very slightly. The tails from the SCL off cases are a little bit more concerning. The oscillations happen at different times for the TL and 3D cases. However, these oscillations are not seen in experiment, as SCL emission dampens the oscillations. When SCL is on, the slope of the tail for the transmission line simulation is steeper than the tail of the 3D simulation.

I accidentally ran an N_2 fill gas, but instead of killing the simulation, I decided to let it run to see if I was close. The results are very good, as the 3D and TL simulations are very similar at each pressure. In the transmission line 200 mTorr SCL on case, the simulation failed for some reason, but the behavior is mostly modeled. There are clear groupings of peaks at each pressure, and the 3D and TL simulations align quite well. Although the oscillations are not perfectly in agreement in SCL off cases, they are closer than oscillations with a Ne fill gas.

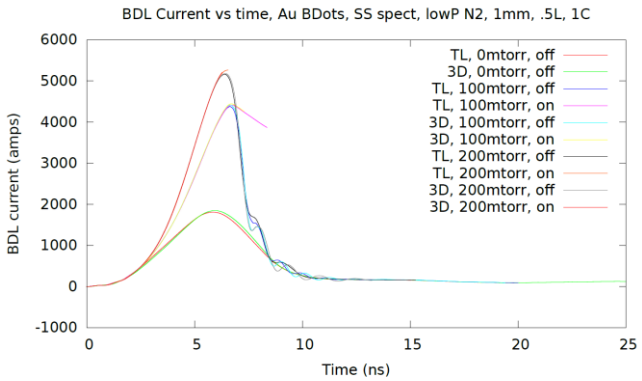

Figure 4.43 Bdl current vs time for a 1 mm B-Dot with the circuit modeled as an axial transmission line with low pressures of N_2 fill gas. SCL ON/OFF.

The following Figures are for high pressure (300-500 mTorr) fill gasses, for both the stainless-steel and silver spectra. These current outputs are for 1 mm B-Dot systems, where transmission line output is compared to full simulation output, and SCL is toggled on and off. The higher-pressure simulations do not produce as accurate of results as the low-pressure simulations, but the pulse shape and pulse width are similar in both cases.

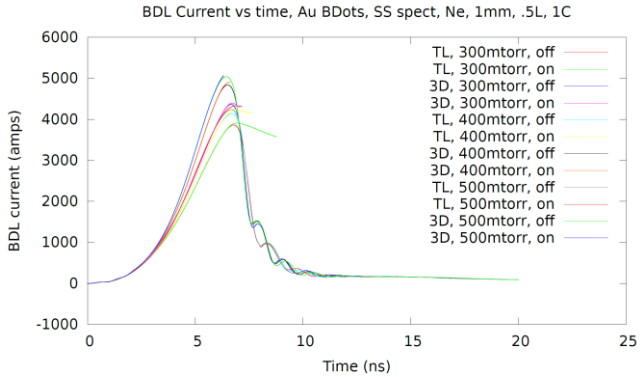

Figure 4.44 Bdl current vs time for a 1 mm B-Dot with the circuit modeled as an axial transmission line with high pressures of Ne fill gas. Capacitance is as calculated, inductance is half the calculated value, SCL ON/OFF.

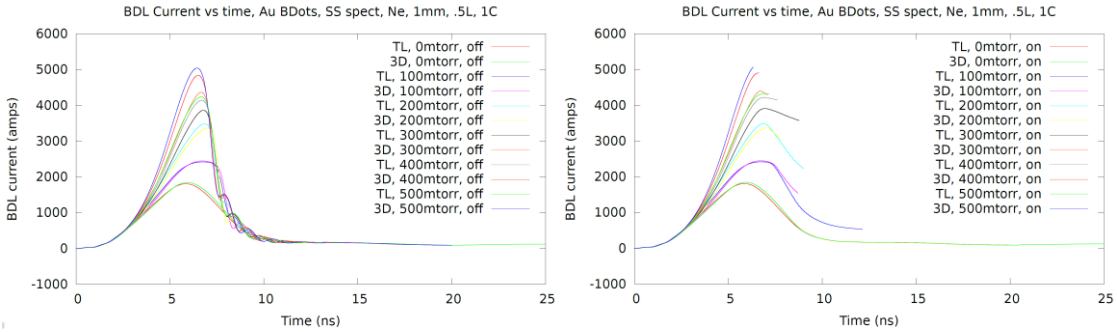

Figure 4.45 Bdl current vs time for a 1 mm B-Dot with the circuit modeled as an axial transmission line with high pressures of Ne fill gas. Capacitance is as calculated, inductance is half the calculated value, SCL ON/OFF separated.

The silver spectrum outputs also used the transmission line parameters from Table 4.3, and the transmission line results are compared to the full 3D simulation. We see that the oscillations after the initial pulse matches. This is what we expected because L and C were calculated to ensure that the oscillation period matches simulation data. The transmission line simulations are underpredicting the peak current at each pressure, however, it is not a significant underprediction, and capturing the oscillatory nature of the cavity accurately is enough compensation for a slightly underpredicted peak current.

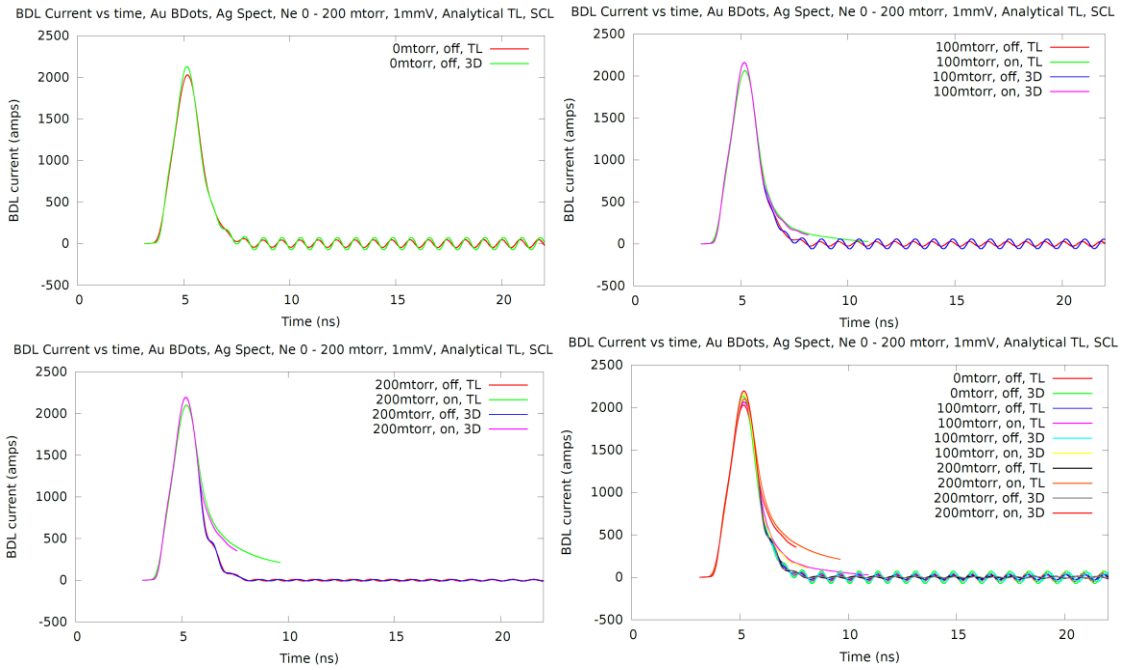

Figure 4.46 Bdl current vs time for a 1 mm B-Dot with the circuit modeled as an axial transmission line with low pressures of Ne fill gas. SCL ON/OFF.

After exploring the Bdl current outputs for low-pressure cavity gap gas fills, it is important to see if the high-pressure cases show similar behavior. Below is the Bdl current outputs for high-pressure Ne fill gas with a silver input spectrum. There is a good

match in rise and fall time between full simulations and transmission line simulations at each pressure, however, the oscillations in the tail and the peak current are slightly off in terms of amplitude. However, for a Ne fill gas modeling a transmission line where the circuit should be seems to be a mostly accurate way to measure current through the system for Ne fill gasses.

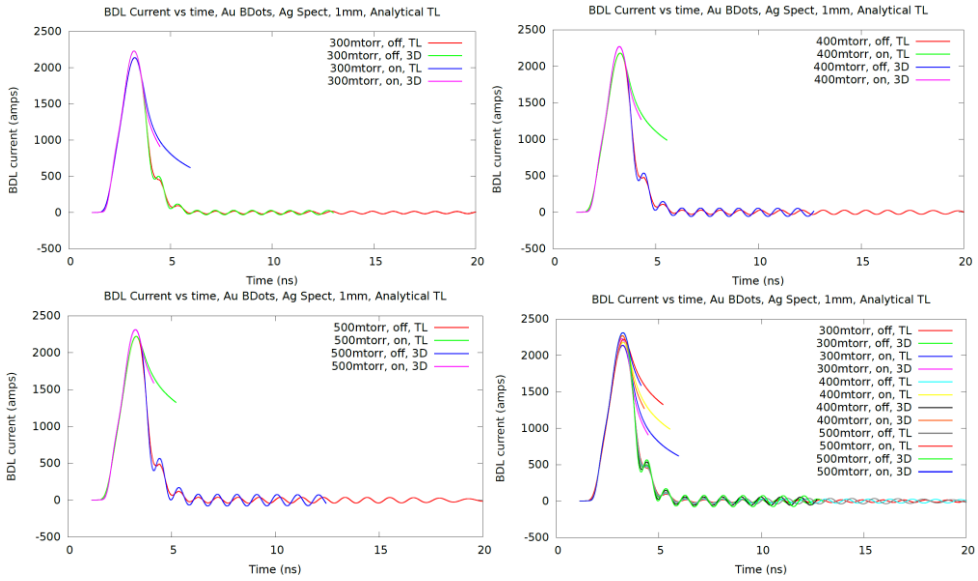

Figure 4.47 Bdl current vs time for a 1 mm B-Dot with the circuit modeled as an axial transmission line with high pressures of Ne fill gas. SCL ON/OFF.

Instead of a Ne fill gas, high-pressure N_2 fill gas was applied in the following simulations for a 1mm stainless steel input spectrum. N_2 is more complex than Ne in that it's diatomic. Simulations crashed for many SCL on cases very early, and the data is incomplete, but the fit seems to be incomplete for high-pressure N_2 fill gas. The reason as to why these simulations are crashing is unknown, but our theory is that the mesh is

overly refined, and the timestep is not reduced enough to compensate for an overly refined mesh.

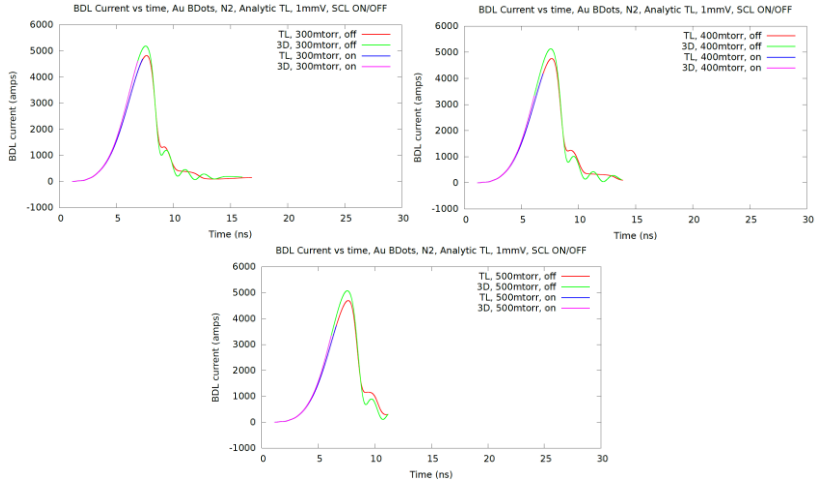

Figure 4.48 Bdl current vs time for a 1 mm B-Dot with the circuit modeled as an axial transmission line with high pressures of N_2 fill gas. SCL ON/OFF.

Even with a much finer mesh, the simulations ran faster for the transmission line cases than for the 3D simulation with the same Courant factor (timestep), as expected. The transmission line simulations require many fewer nodes, and vacuum cases finish in about an hour using only a couple of nodes. So “calibrating” the inductances is not as inconvenient as first thought. Below are the outputs for the 10 mm B-Dot stainless-steel and silver spectra. For stainless-steel, the current outputs match the expected value as pressure increases, which is quite surprising. The pulse shape from the transmission line matches the 3D simulation, but the magnitudes of the peak currents and the slight oscillations are still not accurate. For the silver spectrum, the pulse shape is the same width, but its shape is missing crucial oscillations present in the simulation. Using an

analytically matched transmission line from the 1 mm simulation is not a valid way to measure the current outputs for the 10 mm silver spectrum. The following Figures support this statement.

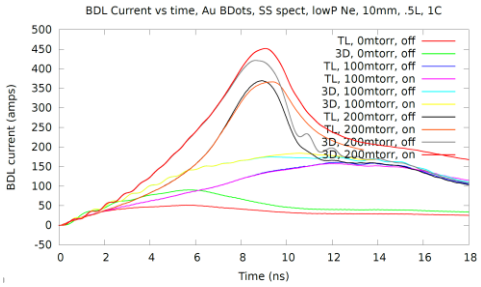

Figure 4.49 Bdl current vs time for a 10 mm B-Dot with the circuit modeled as an axial transmission line with low pressures of Ne fill gas and a stainless-steel spectrum. SCL ON/OFF.

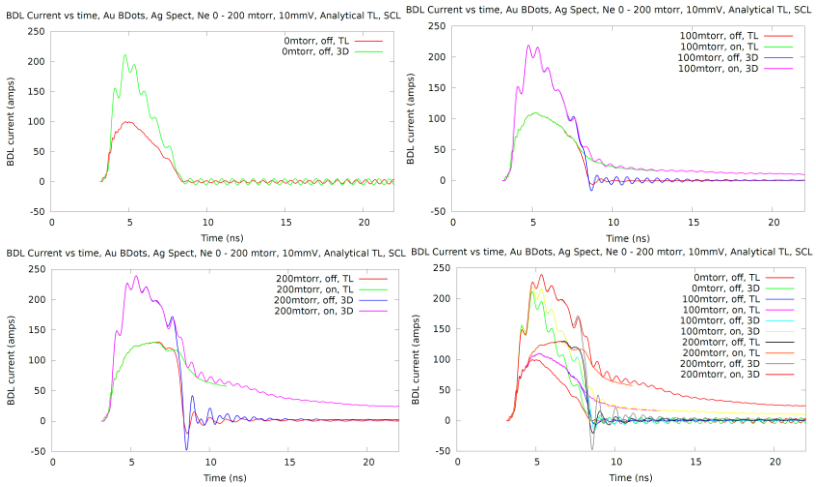

Figure 4.50 Bdl current vs time for a 10 mm B-Dot with the circuit modeled as an axial transmission line with low pressures of Ne fill gas and a silver spectrum. SCL ON/OFF.

The reason that the 10 mm cavities are so inaccurate for silver and stainless-steel input spectra is because of the large SCL emission effects in the cavity. The transmission

line does not accurate capture the physics of these rather large cavities. As shown above, changing the LC values do not have the desired effect, as they do in the 1 mm cases. The stainless-steel spectrum has many low energy (~ 1 keV) photons, which are hard to model in the EM PIC code. Coupled with SCL emission, this makes the behavior very challenging to model. Future work is modeling large cavity gap space-charge limited cavities with a transmission line. In experiment, a 1 mm gap is more common, so modeling the 1 mm cavity with a fill gas is a big step in the right direction.

4.6. EDL CURRENTS: VOLTAGE IN THE CAVITY

Electric potential (voltage) is the integral of electric field over a given length, dl. Edl current graphs measure the voltage within the AK gap. As shown in the Figures below, SCL effects have little to no impact on Edl peak currents. However, the pulse tails of the SCL on cases are slightly higher the SCL off cases due to LC underdamped oscillations.

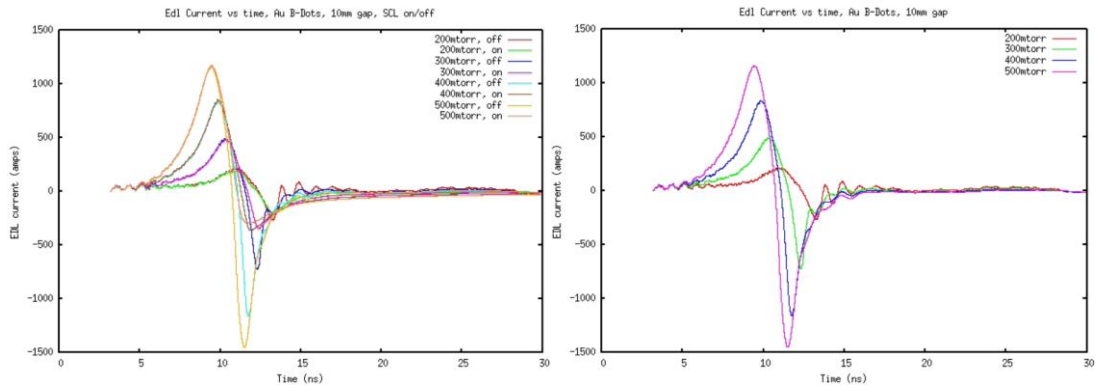

Figure. 4.51 (left) Edl Current vs time for Ne between 200 and 500 mTorr for a 10 mm Au B-Dot system with SCL emission toggled on/off.

As expected for N_2 fill gas, the peak voltage is higher than the peak voltage for Ne, but it peaks at 300 mTorr. This is again due to the required voltage for electric discharge increasing after 300 mTorr, as shown in the Paschen curve.

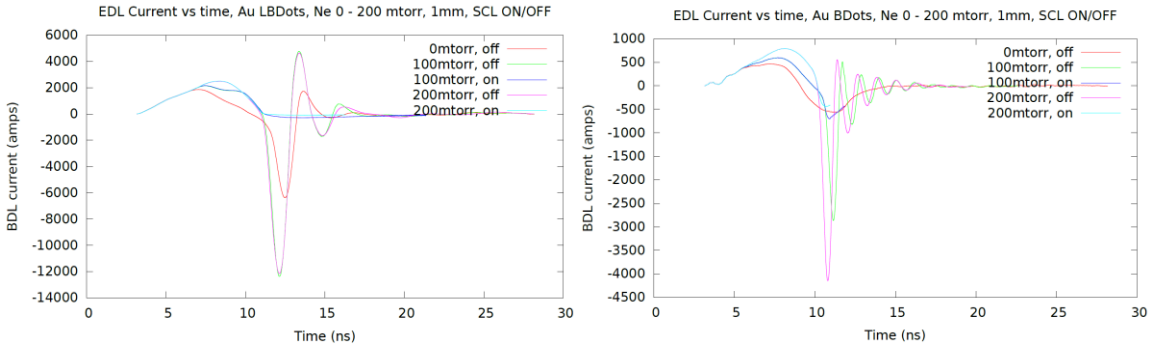

Figure 4.52 Edl Current vs time for Ne between 0 and 200 mTorr for a 1 mm Au LB-Dot (left) and B-Dot (right) system with SCL emission toggled on/off.

4.7. ELECTRIC DISCHARGE AND DOUBLE PEAKS

For some of the SCL off cases, we can see a double peak in the current output (for example, N_2 SCL off case in Figure 4.10, N_2 100 mTorr). Due to the background pressure in the simulation, it takes more time for the gas to become ionized, and the second peak is when the current catches up. There is an inductive effect at higher pressures that creates the second peak. We expect to see another double peak at 24ns, but I chose to run my simulations for N_2 until 20ns because I am more interested in peak current data. Another observation from the simulation results is that the current peaks earlier for the N_2 fill gas than for Ne. The peak is also broader. The N_2 fill gas ionizes earlier than Ne and has more total ionizations; hence, the current with N_2 fill gas is higher. This is true until N_2 surpasses the minimum in the Paschen curve, and it takes more energy to ionize the

gas. After 400 mTorr, N_2 ionizes faster than Ne, but it neutralizes quicker than and tails off before achieving high currents. N_2 has a higher collision frequency cross section at the peak, which explains the broadness, magnitude, and earliness of the peak current. Double peaks are more pronounced when the spectrum is unfiltered. If one were to forget to add the carbon coating to the anode (surface 1, aluminum), then contributions from the anode emission contributes to more pronounced double peaks.

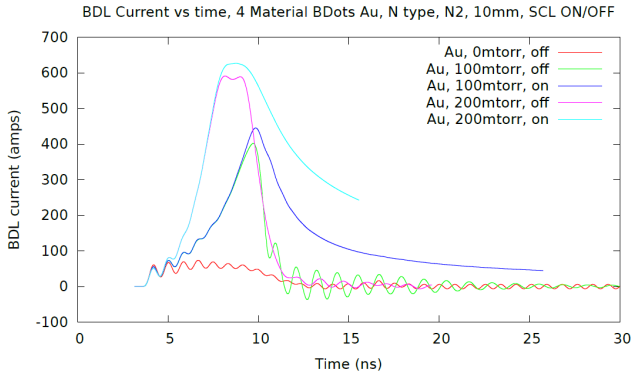

Figure 4.53 Bdl current vs time for N_2 and Ne B-Dot simulations between 0 and 200 mTorr with SCL on/off.

The final Figure shows a more prominent double peaking effect in 200 mTorr of N_2 gas. The input spectrum is stainless steel, but the spectrum is not filtered by the carbon like the rest of the simulations in this work. This leads to higher surface 1 (anode) emission and changes the photocurrents in the B-Dot. The one surface emission assumption is no longer valid, and the emission from the anode contributes to a delayed second peak when SCL is not modeled. The following Figure shows these double peaks for the SCL off case (not shown in the SCL on case because plasma is driving a current

after the initial pulse) for many cathode materials, with silver and gold being the strongest photoelectron emitters.

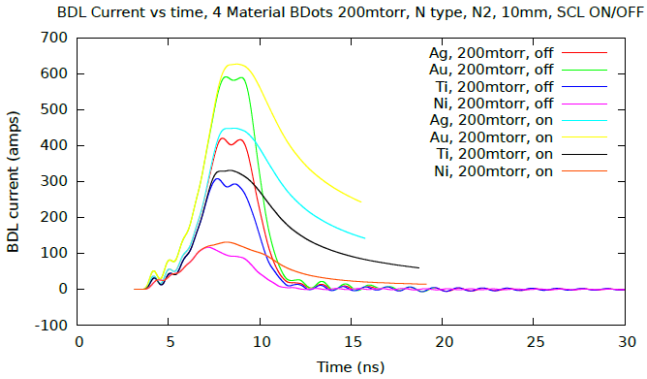

Figure 4.54 Bdl current vs. time for many materials (cathodes) with an N_2 fill gas, SCL on/off. This spectrum (anode) is unfiltered in the MC electron/photon code, so SCL off cases have clear double peaks independent of material [22].

5. DISCUSSION

5.1. DRIVEN AK GAPS AND OTHER DIAGNOSTICS

The simulations were used to calculate Bdl current for a B-Dot diagnostic. However, the EM PIC code is capable of many more things than just modeling B-Dots. If the photoemission cavity acts as an LC circuit, we can somewhat easily switch the diagnostic.

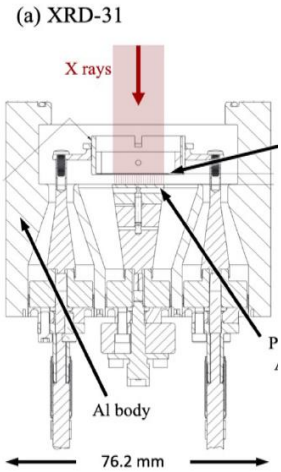

Figure 5.1 DANTE II geometry. X-rays are incident upon the puck at the top of the cavity. It is important to get the geometry and physics of the puck correct in the simulation, but the circuit around the puck (everything that is not the puck in the sketch) can be modeled as an EM circuit [23].

For example, let's look at XRD-31 (DANTE II) at the National Ignition Facility (NIF). The diagnostic is relevant to the work done in the B-Dot because it is an 18-energy channel warm x-ray diagnostic (.05 – 20 keV) that can measure time-dependent current, voltage, system temperature, and photon flux [23]. The raw data is x-ray power, but with

some simple data transformation, we can model our desired output. Instead of the Z-pinch Stainless-Steel wire array used on the Z machine at Sandia, I was provided data for an Ag and Cu spectrum from experimental data, and the input photon spectrum MC photon/electron transport code can be changed to a spectrum used at NIF. Below is the geometry of the DANTE II diagnostic. The puck is where the photons come in and where the emission surfaces are (top of the Figure). Just like the Stainless-Steel spectrum, filters (Kapton, Lithium, Tantalum, etc.) can be added to the input spectra to obtain a spectrum in our desired energy range.

However, modeling a diode's AK gap physics is not as trivial as changing the geometry. The B-Dot has one dominant emission surface, the Au cathode (which can be changed to a different material, but this simulation focused on gold). For DANTE II to have one emission surface, it must be driven. This means that there is an external applied voltage across the gap, which is different than the B-Dot simulation. As briefly mentioned in the background information section 2.5, adding a voltage changes the charge and current (both as a function of time) behavior, as we are solving a heterogenous differential equation instead of a homogenous differential equation. In the EM PIC code, the driven voltage can be set in the initial conditions block.

The importance of using a transmission line to model the non-plasma physics parts of the simulation not only reduces computation time, but it allows us to change the detector with relative ease. An XRD and a B-Dot are different diagnostics, but when switching between the two diagnostics, the only things that change are the input geometry (along with the sidesets, boundary conditions, meshing, etc.) and the voltage across the gap. Depending on the machine and the target, the input spectrum would also change.

Just like the B-Dot can output Bdl or Edl currents (current and voltage in the gas filled cavity), the XRD can also output current and voltage. The physics modeled in the XRD, or other diagnostic, would not change; however, modeling a transmission line in place of the return circuit is where this method has its merits. As shown in Figure 5.1, the return circuit for XRD-31 is very complex. To model it as a transmission line, all that is needed are the calculated L and C per unit length from the coaxial cable equations. Although I studied the XRD as an alternate diagnostic, future work could be to repeat this AK gap simulation for different X-ray diagnostics on NIF, the Z machine (or other pulsed power facilities at Sandia), or even the International Thermonuclear Experimental Reactor (ITER) in France.

5.2. COUPLING THE MC CODE TO THE EM PIC CODE

Coupling the MC photon/electron code to the EM PIC code in this simulation is integral in understanding the physics of the photoemission driven cavity. The MC photon/electron code is needed to produce a photoelectron spectrum that the EM PIC code uses (along with time pulse data) to calculate important physics of the system, but there are other ways to perform these calculations. The EM PIC code can take a single energy of photoelectrons without the MC code, but using a spectrum provides a more comparable photon spectrum to experiment. The B-Dot cavity system is also not a fully three-dimensional system, even though the MC photon/electron code can be run in 1-D, 2-D (cylinder), or 3-D. It would be interesting to explore how the EM PIC code's current outputs change when different dimensions of the MC photon/electron code are used as

the input spectrum. However, we choose to use our MC photon/electron code and couple it to the EM PIC because the structure exists to move between the two codes very easily.

5.3. APPLICATIONS

The applications of this research are in modeling x-ray diagnostics while reducing computational resources, but it also has applications to nuclear deterrence. It is essential to know that the nations systems will be safe, secure, and effective in harsh environments, including environments of high-energy short-pulsed x-rays. It is important to know how SCL emission effects current in systems that have an AK gap. Air is about 80% N_2, so the N_2 simulations would be most applicable to systems found outside of a lab. We notice that just a pressure changes of 200 mTorr changes the peak current in the cavity by an order of magnitude, but we also discovered that the voltage required for electric discharge increases after 300 mTorr and suppresses peak current. Radiation hardening equipment will always be important in ensuring functionality of equipment, and these simulations provide important data for x-ray irradiated materials. Understanding SCL emission also has applications in plasma physics of ablators (heat shields) and objects in orbit with electrical systems.

6. CONCLUSION

This work explored simulations of radiation transport in cylindrical end irradiated photoemission cavities with a B-Dot diagnostic. The B-Dot measures the change in magnetic field in time induced by a current. The photoelectric effect, SCL emission, electric discharge, LC circuit modeling, and MC methods were discussed as precursors for the simulations. A MC photon/electron radiation transport code irradiated an AK gap, where the anode was carbon coated Aluminum, and the cathode was gold. Convergence testing was also performed to optimize the number of particles required for similar simulations.

After obtaining a photoelectron emission spectrum from each surface, we used an EM PIC kinetic plasma code to model Bdl and Edl current outputs. A comparison of Ne and N_2 fill gasses was performed, and we saw that Ne's minimum voltage required for electric discharge is much higher than N_2's, but N_2 has a higher peak current, and its current peaks earlier. N_2's peak current decreases after 300 mTorr because of effects seen in the Paschen curve.

The full 3D simulation was compared to modeling the system in two parts: the gas filled cavity and a transmission line. It was shown that modeling a transmission line as an LC circuit coupled with the cavity's photoelectric emission produced similar results to the full 3D experiment, and modeling parts of an EM simulation as a transmission line is a viable method of reducing computational resources without sacrificing accuracy. The key is to bring in the transmission line axially instead of radially.

There are many ways to calculate the LC values for the transmission line. Once we realized that 10mm gap sizes are not sensitive to changes in R, L, or C, we switched to modeling the EM circuit of a 1mm cavity. The first attempt was to use the equation for a coaxial cable to find the capacitance and inductance per unit length of a capacitor. We found the rise times, peak currents, and tail oscillations to not match experimental data, so we changed the inductance and capacitance until we found a solution that closely matched our experiment. Halving the inductance in the calculated values of our transmission line is required because the calculated values of L per unit length model the inductance twice from the EM pulse. This caused our results improved significantly, but there was still an opportunity to improve our output current rise time and oscillation frequency. From the post-time pulse oscillation frequency of the silver spectrum, we can calculate L and C. Once we changed the LC value accordingly in our simulation, we found much more accurate rise times, peak currents, and post-time pulse oscillation frequencies.

After finding these values from the silver spectrum, it is important to know if these values are calibrated to only silver's x-ray yield and time pulse, or if they are accurate for the stainless steel-spectrum as well. Simulations were run for the stainless-steel spectrum with the silver LC values, and the pulse shapes looked very similar. When applying this to higher pressure simulations, we found better matching in 1mm gap sizes for N_2 than Ne, but the results were similar enough to conclude that transmission line modeling for the EM circuit is a viable way to measure output currents in a photo-emission driven cavity. However, for 10mm cases, it is apparent that LC parameters are not the dominant physics of the system, as it is highly space-charge limited.

Future work for this project would be to change different parts of the experiment and compare the results to experiment. This would include changing the material of the cathode surface to a similar metal to gold (silver or copper), while keeping the anode and filter stack the same. Since we want to limit anode emission, keeping this surface the same can help us directly compare different irradiation material Another avenue of work is changing the input x-ray spectrum in the MC photon/electron code, and seeing how that changes AK photoemission spectra from each surface, and its subsequent effect on Bdl current outputs for a B-Dot. Finally, the most promising line of future work would be modeling the DANTE II diagnostic instead of a B-Dot. The experiment would be very similar to the B-Dot experiment but adding the external voltage to the gap changes the physics of the simulation. It would be a further proof of concept that the EM PIC code can model the EM parts of the geometry as an LC or RLC circuit. We could also go back and add dampening (resistance) to our EM PIC code input (create an RLC transmission line) and compare results to the LC circuit transmission line. The work I plan to pursue is adding temperature depending on photoemission effects to the irradiated surface.

APPENDIX

SIMULATION OF LC CIRCUITS IN CYLINDRICAL PHOTOEMISSION DRIVEN CAVITIES USING COUPLED MONTE CARLO AND PARTICLE-IN-CELL CODES

Table A.1 N_2 peak currents and differences between the previous pressure in 100 mTorr bins.

Pressure (mTorr)	SCL OFF/ON	Peak Current (A)	Difference Between Previous Pressure and SCL
100	Off	880	788
100	On	953	861
200	Off	2443	1563
200	On	2611	1658
300	Off	2876	433
300	On	3251	640
400	Off	2961	85
400	On	3267	16
500	Off	2783	-178
500	On	2894	-373

Table A.2 Ne peak currents and differences between the previous pressure in 100 mTorr bins.

Pressure (mTorr)	SCL OFF/ON	Peak Current (A)	Difference Between Previous Pressure and SCL
100	Off	180	88
100	On	195	103
200	Off	426	246
200	On	471	276
300	Off	786	360
300	On	902	431
400	Off	1294	508
400	On	1432	530
500	Off	1734	440
500	On	1856	424

Table A.3 Transmission line data for B-Dot geometry brought in axially.

#Length	num_cells	C_l	L_l	G_l
0.002	20.0	5.910195817843425e-11	1.882594232655415e-07	0.0
0.011	110.0	5.910195817843425e-11	1.882594232655415e-07	0.0
0.01	100.0	6.889189348252632e-12	1.6150667368952925e-06	0.0
0.005	50.0	1.1705623268286148e-10	9.505261108719454e-08	0.0
0.002	20.0	1.1705623268286148e-10	9.505261108719454e-08	0.0

- C_l and L_l are capacitance and inductance per length respectively
  - These were calculated using the formulae in the previous slide
- G_l is conductivity per length
- The lengths (m) are the distances from the TL to the B-Dot cavity in the 3-D simulation

Table A.4 Transmission line data for LB-Dot geometry brought in axially.

```
#LBDot transmission line data file
0.002 20.0  5.910195817843425e-11  1.882594232655415e-07 0.0
0.011 110.0 1.9048946236776195e-12 5.841005808003798e-06 0.0
0.01  100.0 1.5309282688373993e-12 7.267813121633549e-06 0.0
0.005 50.0  1.935784561815264e-12  5.747798995825451e-06 0.0
0.002 20.0  1.1705623268286148e-10 9.505261108719454e-08 0.0
```

```
Circuit Network:
  Transmission Lines:
    BDot_body:
      Names: [BDot_body]
      Mode: TEM
      Parameters File: TransmissionLine.dat
  Nodes:
    EM Coupling:
      Type: EM Coupling
      Transmission Lines: [BDot_body]
      Sideset: surface_3
      Conductors: [cathode, anode]
      Ground: cathode
    Voltage Source:
      Type: Open Circuit Source
      Transmission Line: BDot_body
      Resistance: 1.0e-12
      Voltage Source Function: |
        Voc = 0;
```

Figure A.1 Circuit network code block in EM PIC input file. Number of cells is how many points between the mesh boundaries.

```
Time History Diagnostics:
# z_bdot = {z_bdot=-mm2m*height/2}
# The wedge now goes from -wedge_angle/2 to wedge_angle/2 instead of 0 to wedge_angle
# rel_angle = {rel_angle=PI*wedge_angle/180.0}
# radius_bdot = {radius_bdot = mm2m*emission_plate_radius*.995}
# radius_edl = {radius_edl=0.5 * aperture_radius * mm2m}
  EDL:
    Line Integral:
      Field: E
      Points: (0.01, 0, {-mm2m*height}), (0.01, 0, 0.0)
      Num Points: {int(10*height/effective_h + 0.5)}
  BDLCurrent:
    Line Integral:
      Field: B
      Multiplier: {current_scale / permeability}
      Points: ({radius_bdot*cos(0.5*rel_angle)}, {radius_bdot*sin(0.5*rel_angle)}, {z_bdot}), ({radius_bdot*cos(-0.5*rel_angle)}, {radius_bdot*sin(-0.5*rel_angle)}, {z_bdot})
      Num Points: {int(10*2*radius_bdot*sin(0.5*rel_angle)/(mm2m*effective_h )+0.5)}
  BDLCurrent_circle:
    Line Integral:
      Field: B
      Multiplier: {current_scale / permeability}
      Circle Center: 0,0, {z_bdot}
      Circle Radius: {radius_bdot}
      Circle Normal: 0, 0, -1
```

Figure A.2 Diagnostic block from EM PIC code. These blocks compute the current and voltage in different parts of the geometry, TL stands for transmission line.

Table A.5 Transmission Line Data for the B-Dot geometry calculated from oscillation period.

#Length	num_cells	C_l	L_l	G_l
0.002	20	1.003492148e-10	6.852643008e-08	0.0
0.011	110	1.003492148e-10	6.852643008e-08	0.0
0.01	100	1.979256108e-11	3.474322207e-07	0.0
0.005	50	1.987497774e-10	3.459915044e-08	0.0
0.002	20	1.987497774e-10	3.459915044e-08	0.0

BIBLIOGRAPHY

[1] P. J. Christenson, T. M. Flanagan and K. L. Cartwright, "EMPIRE Simulations of the July 2020 photoelectron driven cavity B-Dot experiments at the National Ignition Facility," no. SAND2021-11895, 2021.

[2] T. Huiskamp, F. J. Beckers, E. J. v. Heesch and e. Al, "B-Dot and D-Dot Sensors for (Sub)Nanosecond High-Voltage and High-Current Pulse Measurements," *IEEE SENSORS JOURNAL,* vol. 16, no. 10, pp. 3792 - 3801, 2016.

[3] R. Piejak, V. Godyak and B. Alexandrovich, "The electric field and current density in a low-pressure inductive discharge measured with different -dot probes," *Journal of Applied Physics,* vol. 81, pp. 3416 - 3421, 1996.

[4] X. He, J. X, F. Sun. and e. al, "Modeling and Tests of Nested Transmission Lines for Current Adding ona Four-Stage Linear Transformer Driver," *Rev. Sci. Instrum.,* vol. 93, p. 11, 2022.

[5] T. Flanagan, K. Bell, C. Turner, P. Christenson, T. Zarick and R.R. Romero, "Underdamped Resonant Oscillations in a Simple SGEMP Cavity," *Journal of Radiation Effects,* vol. 39, no. 1, pp. 82-91, 2021.

[6] A. Tochino, Y. Komori and T. Mitsui, "Integration of the stochastic underdamped harmonic oscillator by the Theta Method," *Mathematiics and Computers in Simulation,* vol. 199, pp. 217-230, 2022.

[7] A. L. Garner, G. Meng, Y. Fu and e. Al., "Transitions between electron emission and gas breakdown mechanisms across length and pressure scales," *Journal of Applied Physics,* vol. 128, pp. 210903-1 - 21090324, 2020.

[8] S. Klassen, "The Photoelectric Effect: Reconstructing the Story for the Physics Classroom," *Sci & Educ,* vol. 20, pp. 719 - 731, 2011.

[9] R. J. Umstattd, C. G. Carr, C. L. Frenzen and e. al., "A simple physical derivation of Child–Langmuir space-charge-limited emission using," *American Journal of Physics,* pp. 160-163, 2005.

[10] T. C. Powell, "Theory, Simulation, and Experiments on a Magnetically Insulated Transmission Line Terminated by a Bremsstrahlung Diode," *University of New Mexico Depatment of electrical and Computer Science,* 2023.

[11] A. M. Darr, A. M. Doveless and A. L. Garner, "Unification of field emission and space charge limited emission with collisions," *Applied Physics Letters,* vol. 114, pp. 014103-1 - 014103-5, 2019.

[12] M. A. Lieberman and A. J. Lichtenberg, Principles of plasma discharges and materials processing (2nd ed.), Hoboken, N.J.: Wiley-Interscience, 546, 2005.

[13] L. F. Berzak, S. E. Dorfman and S. P. Smith, "Paschen's Law in Air and Noble Gasses," *Lawrence Berkely National Labs,* 2006.

[14] C. A. Balanis, Advanced Engineering Electromagnetics, John Wiley & Sons, 2012.

[15] W. McAllister, "LC Natural response," *Khan Academy,* 2023.

[16] M. H. Nayfeh and M. K. Brussel, Electricity and Magnetism, New York, NY: John wiley & Sons, 2015.

[17] R. L. Harrison, "Introduction f Monte Carlo Simulations," *American Institute of Physics,* vol. 1204, pp. 17 - 27, 2010.

[18] M. T. Bettencourt, D. A. S. Brown, K. L. Cartwright and e. Al, "EMPIRE-PIC: A Perfrmance Portable Unstructured Particle-in-Cell Code," *Communications in Computational Physics,* 2021.

[19] D. J. Griffiths, Introduction to Electrodynamics, Fourth Edition, Glenview IL: Pearson, 2013.

[20] P. Hillion, "The Courant–Hilbert solutions of the wave equation," *Journal of Mathematical Physics,* vol. 33, no. 8, pp. 2749-2753, 1992.

[21] H. C. Hayden and N. G. Utterback, "Ionization of Helium, Neon, and Nitrogen by Helium Atoms," *Physical Review,* vol. 135, no. 6A, pp. 1575 - 1579, 1964.

[22] R. Shastri, "Simulating Space Charge Limited Emission Effects in Photoemission Driven Cavities Final," no. SAND_1677996, pp. 1-11, 2022.

[23] G. E. Kemp, M. J. May, L. P. MacNeil and e. Al., "A compact filtered x-ray diode array spectrometer for the National Irradiation Facility: SENTINEL," *Review of Scientific Instruments,* vol. 91, pp. 123502-1 123502-8, 2020.

VITA

Ravi Sanjay Shastri was born in Saint Louis, Missouri, and he has lived there for most of his life. In December 2020, he graduated from Missouri S&T with a bachelor's degree in physics. He continued his education as a master's student in the Nuclear Engineering and Radiation Sciences Department at Missouri S&T, and he will pursue his Ph.D. in Nuclear Engineering and Radiation Sciences at the Rackham College of Engineering at the University of Michigan upon completion of his masters in July 2023.

At Missouri S&T, Ravi was involved with Delta Sigma Phi Fraternity's programming branch, Missouri S&T's Residential Life, American Nuclear Society, Spanish Club, ΣΠΣ, Jazz Combo, Symphonic Orchestra. He was the vice president of the American Nuclear Society, ANΣ, and the Spanish Club, and he was concertmaster of the wind symphony. He thanks you for reading this work.